mathematics

Article

Static-Aperture Synthesis Method in Remote Sensing and Non-Destructive Testing Applications

Olha Inkarbaieva [1], Denys Kolesnikov [1], Danyil Kovalchuk [1], Volodymyr Pavlikov [1], Volodymyr Ponomaryov [2,*], Beatriz Garcia-Salgado [2], Valerii Volosyuk [1] and Semen Zhyla [1]

[1] Aerospace Radio-Electronic Systems Department, National Aerospace University "Kharkiv Aviation Institute", 61070 Kharkiv, Ukraine; o.inkarbayeva@khai.edu (O.I.); d.kolesnikov@khai.edu (D.K.); d.i.kovaljchuk@khai.edu (D.K.); v.pavlikov@khai.edu (V.P.); v.volosyuk@khai.edu (V.V.); s.zhyla@khai.edu (S.Z.)
[2] ESIME Culhuacan, Instituto Politecnico Nacional, Mexico City 04330, Mexico; bgarcias1404@alumno.ipn.mx
* Correspondence: vponomar@ipn.mx

Abstract: The study is dedicated to the statistical optimization of radar imaging of surfaces with the synthetic aperture radar (SAR) technique, assuming a static surface area and applying the ability to move a sensor along a nonlinear trajectory via developing a new method and validating its operability for remote sensing and non-destructive testing. The developed models address the sensing geometry for signals reflected from a surface along with the observation signal–noise equation, including correlation properties. Moreover, the optimal procedures for coherent radar imaging of surfaces with the static SAR technology are synthesized according to the maximum likelihood estimation (MLE). The features of the synthesized algorithm are the decoherence of the received oscillations, the matched filtering of the received signals, and the possibility of using continuous signal coherence. Furthermore, the developed optimal and quasi-optimal algorithms derived from the proposed MLE have been investigated. The novel framework for radio imaging has demonstrated good overall operability and efficiency during simulation modeling (using the MATLAB environment) for real sensing scenes. The developed algorithms of spatio–temporal signal processing in systems with a synthesized antenna with nonlinear carrier trajectories open a promising direction for creating new methods of high-precision radio imaging from UAVs and helicopters.

Keywords: remote sensing; non-destructive testing; SAR systems; static-aperture synthesis; coherent image; maximum likelihood estimation

MSC: 60G35; 68U10

Academic Editor: Konstantin Kozlov

Received: 9 January 2025
Revised: 30 January 2025
Accepted: 31 January 2025
Published: 3 February 2025

Citation: Inkarbaieva, O.; Kolesnikov, D.; Kovalchuk, D.; Pavlikov, V.; Ponomaryov, V.; Garcia-Salgado, B.; Volosyuk, V.; Zhyla, S. Static-Aperture Synthesis Method in Remote Sensing and Non-Destructive Testing Applications. *Mathematics* **2025**, *13*, 502. https://doi.org/10.3390/math13030502

1. Introduction

Systems operating in different wave bands, such as optical [1,2], infrared [3,4], or radio [5,6], are used to obtain images of studied objects or areas. Each of these bands has its characteristics, a specific field of application, and different degrees of development of the component base. Moreover, they can be used separately or in combination with others [7–9]. Despite the larger dimensions of radio systems compared to optical and infrared sensors, radio imaging systems have improved for over 50 years. The importance of radio systems is associated with the following advantages of the radio band: low dependence on weather conditions and independence from the time of day, illumination, and the presence of high informational content of electromagnetic waves scattered by the surface. In earth surface exploration applications, the SAR systems are the most developed [10–12]. Those systems are installed on space (or airborne) carriers. They can be used not only as mapping systems but also in the study of the underlying surface [13], in monitoring the state of natural resources [14], tracking the state of agricultural areas [15], and studying and preventing environmental disasters [16], among others. The spatial resolution of the restored SAR images can reach decimeter resolution from low-orbiting satellites, which is comparable to the same satellites' optical systems.

Another area of studying objects in the radio band frequencies consists of systems that generate and process signals according to aperture synthesis technology [17,18]. The most widespread and developed are ground-based interferometric systems used in studying space objects and in radio telescopes [19,20]. In such systems, the angular resolution reaches milli-arcseconds or even micro-arcseconds.

Global radiovision from aerospace platforms represents a challenge addressed using different approaches, such as models developed using laboratory settings or anechoic chambers to conduct static experiments to localize objectives [21–23]. The generation of representative test imagery for surfaces, ground-based structures, aircraft, and various technological systems remains a pressing concern [24–26]. Furthermore, the advancement of technologies for designing components, devices, and assemblies with integrated capabilities for non-destructive testing is continually progressing [27–29]. These systems enable novel approaches to remote testing by optimizing testing environments, trajectory configurations, and measurement equipment, encompassing diverse wavebands, antenna designs, and operational modes.

Space-based systems cannot solve (or can solve with certain limitations) the tasks of local radiovision. They are cumbersome, have too much weight, rely on the Earth's orbit and rotation, and their imaging algorithms depend on a high altitude above the measured area. In the case of ground-based aperture synthesis systems, it is necessary to have spatial bases between the radio telescopes of around tens of kilometers to obtain high resolution. Also, there is a dependence on the Earth's rotation to fill in the spatial frequencies of the restored images.

Over the past decades, many SAR systems have been implemented to acquire images of objects located within close range of the system [30–33]. However, such systems' disadvantages are their large size, design based on engineering experience and opinion, and the lack of an optimization problem. Also, these systems can realize a strictly side view only when the carrier moves in a straight line. In contrast, modern systems, such as Unmanned Aerial Vehicles (UAVs) or software-defined scanning devices, can change their position and direction of movement quite abruptly, i.e., the motion trajectory can be nonlinear. In this case, the movement trajectory can serve as an additional source of information, contributing to enhanced image resolution. Moreover, this feature can also support signal modulation, the application of Multiple-Input Multiple-Output (MIMO) principles in antenna design, and the integration of separate spatially distributed antennas within systems of interferometric aperture synthesis.

Thus, a contradiction arises: implementing the classical SAR algorithm in the laboratory by multiple passes is quite time-consuming, and the range resolution is insufficient. Aperture synthesis methods also cannot be placed in an anechoic chamber due to the large areas of antenna deployment, and coherent processing is also expensive. At the same time, radio engineering systems for forming radio images of a static scene from small distances and conditions in the laboratory are relevant and require further development.

Resuming the drawbacks of the exposed literature approaches: An important scientific problem exists in developing statistical methods and algorithms for forming high-resolution radio images of static areas and performing some practical implementations of proposed techniques in remote sensing and non-destructive testing systems. This study is focused on solving the mentioned problems. The principal contributions of this study are as follows:

1. Theoretical models of sensing, exploration of the sensing geometry for signals reflected from the surface, along with a signal–noise equation that includes correlation properties.
2. MLE algorithms are used for coherent radar imaging of surfaces in static SAR technology.
3. Simulation modeling of the designed radar imaging for real sensing scenes that justifies good general operability and efficiency.

2. Materials and Methods

This section presents the statistical optimization of the radar system structure for imaging surfaces with the technology of static-aperture synthesis. The section considers the observation geometry of a static surface area by a radar moving at a specific height along nonlinear trajectories for further signal processing and formation of a high-resolution surface image. The models of the received informative signals, internal noise, observation equations, and their correlation properties are defined. Furthermore, optimal and quasi-optimal methods of radio image formation with the static-aperture synthesis technology are obtained. Based on the developed method, algorithmic operations are proposed, and a signal processing block diagram is developed. Moreover, potential accuracies of forming a radio image of a surface are investigated.

2.1. Geometry, Signal–Noise Models, and Observation Equation

2.1.1. Geometry

Let us assume that a radar sensor as a high-frequency transmitting and receiving path with an antenna whose surface is described by the coordinates $\vec{r}'$ moves along an arbitrary trajectory parallel to the x, y plane and emits a sensing signal in a wide sector of angles:

$$s_t(t) = A(t)cos(2\pi f_0 t + \phi) = Re\left\{\dot{A}(t)e^{j\omega_0 t}\right\}, \tag{1}$$

where $\dot{A}(t) = A(t)e^{j\Phi}$ is the sensing signal's complex envelope; $A(t)$ is the sensing signal's amplitude; ϕ is the initial phase; $\omega_0 = 2\pi f_0$ is the angular frequency; and f_0 is the frequency.

The complex envelope $\dot{A}(t)$ describes the change in phase and amplitude of the sensing signal. It can take many known models of continuous and pulsed signals, including those with complex intra-pulse modulation, e.g., linear frequency-modulated, phase-shift-keyed, stochastic, among others. Pulse- and multi-frequency modulated signals have a complex envelope of the following form:

$$\dot{A}(t) = \sum_{p=1}^{P} \dot{S}_p(t - pT_P), \dot{A}(t) = \sum_{q=1}^{Q} \dot{S}_q e^{j\omega_q t}.$$

The geometry along which the sensor moves is shown in Figure 1. For further calculations, the following notations are introduced: $\vec{r} = (x, y, z)$ is the coordinate of the surface, $\vec{r}' = (x', y', z')$ is the coordinate of the scattered signal registration area, $d\vec{r} = dxdy$ is an elementary plane on the surface that reflects the sensing signals, $\vec{r_t}$ is the shift of the signal registration area center when the sensor is moved, $\vec{r} - \vec{r_t}$ is the coordinates of the elementary plane $d\vec{r}$, D is the area of all possible surface coordinates, D' is the area of all possible registration area coordinates, D'_p is the area of all possible values of the non-synthesized antenna, H is the height at which observations are made, $\vec{\vartheta} = (\vartheta_x, \vartheta_y)$ is the vector of directional cosines, $R\left(\vec{r}, \vec{r_t}\right)$ is the distance from the center of the scattered signal registration to each point of the surface, and $R\left(\vec{r}, \vec{r}', \vec{r_t}\right)$ represents the distance between any given point within the scattered signal registration area and each corresponding point on the surface.

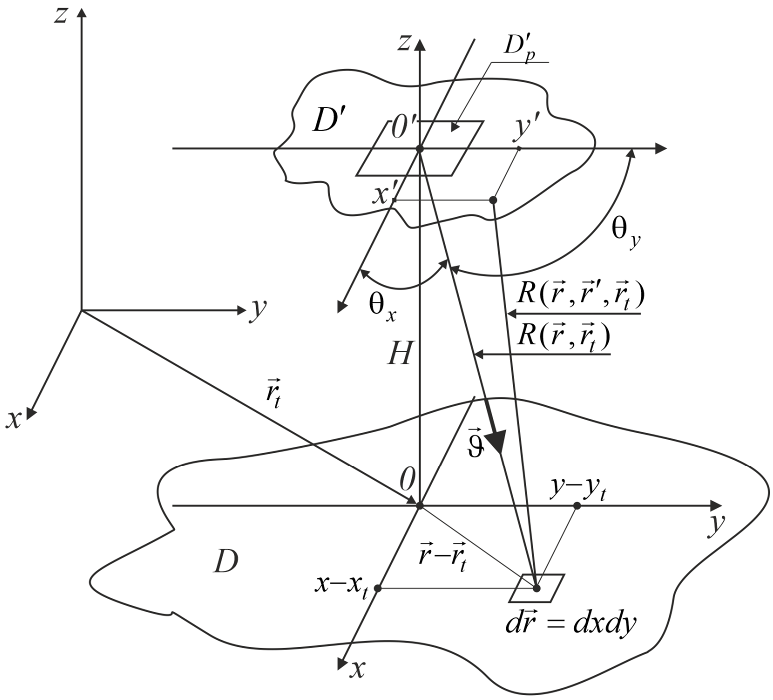

Figure 1. Surface-sensing geometry in static-aperture synthesis of antenna.

2.1.2. Received Signals

Using the phenomenological approach [34] for determining the sensing signals scattered by the surface when the surface is assumed to be statistically homogeneous, we can write the received signals by each point in the registration area as follows:

$$s_r\left(t, \vec{r}', \vec{r_t}\right) = Re\left\{\int_D \dot{F}\left(\vec{r}\right) \dot{s}_0\left(t, \vec{r}, \vec{r}', \vec{r_t}\right) d\vec{r}\right\}, \tag{2}$$

where $\dot{F}\left(\vec{r}\right)$ is a surface coherent image representing the quantitative value of the reflection coefficient of incident waves by each of its points, and

$$\dot{s}_0\left(t, \vec{r}, \vec{r}', \vec{r_t}\right) = \dot{I}\left(\vec{r}'\right)\dot{A}\left(t - t_{\mathrm{del}}\left(\vec{r}, \vec{r}', \vec{r_t}\right)\right)e^{j2\pi f_0\left(t - t_{\mathrm{del}}\left(\vec{r}, \vec{r}', \vec{r_t}\right)\right)}, \tag{3}$$

is a single signal that is expected to be received by each point of the registration area $\vec{r}'$ when the sensor is placed at point $\vec{r_t}$ from each elementary plane $d\vec{r}$ on the surface with coordinates $\vec{r}$, and $\dot{F}\left(\vec{r}\right) = 1$,

$$t_{\mathrm{del}}\left(\vec{r}, \vec{r}', \vec{r_t}\right) = \frac{2R\left(\vec{r}, \vec{r}', \vec{r_t}\right)}{c} \tag{4}$$

is the time taken to propagate the signal from the antenna center (during transmission) to each point of the surface and vice versa, considering the sensor movement along the $\vec{r_t}$ coordinate,

$$\begin{gathered} R\left(\vec{r}, \vec{r}', \vec{r_t}\right) = R(x, y, x', y', y_t, x_t) = \\ \sqrt{H^2 + [x - (x_t + x')]^2 + [y - (y_t + y')]^2}. \end{gathered} \tag{5}$$

Considering the research in Section 1, we can perform all further mathematical operations in the Fresnel zone, using only the quadratic terms when expanding the distance (5) into the Taylor series. For such measurement conditions, we apply the following constraints:

$$\left|x - (x_t + x')\right| \ll H, \left|y - (y_t + y')\right| \ll H, x' \ll H, y' \ll H. \tag{6}$$

Let us develop Equation (5) for the Fresnel zone; see Appendix A.1.

$$\begin{gathered}
R\left(\vec{r}, \vec{r}', \vec{r}_t\right) = R(x, y, x', y', x_t, y_t) = \sqrt{H^2 + [(x - x_t) + x']^2 + [(y - y_t) + y']^2} \\
= \sqrt{\left(R_0\left(\vec{r} - \vec{r}_t\right)\right)^2 - 2(x - x_t)x' - 2(y - y_t)y' + (x')^2 + (y')^2} \\
= R_0\left(\vec{r} - \vec{r}_t\right)\sqrt{1 + \frac{-2(x-x_t)x' - 2(y-y_t)y' + (x')^2 + (y')^2}{\left(R_0\left(\vec{r} - \vec{r}_t\right)\right)^2}} \\
\approx R_0\left(\vec{r} - \vec{r}_t\right) - \frac{(x-x_t)x'}{R_0\left(\vec{r} - \vec{r}_t\right)} - \frac{(y-y_t)y'}{R_0\left(\vec{r} - \vec{r}_t\right)} + \frac{1}{2}\frac{(x')^2}{R_0\left(\vec{r} - \vec{r}_t\right)} + \frac{1}{2}\frac{(y')^2}{R_0\left(\vec{r} - \vec{r}_t\right)}, \\
\text{given } (1 + x)^{\frac{1}{2}} = 1 + \tfrac{1}{2}x - \tfrac{1}{8}x^2,
\end{gathered} \tag{7}$$

where

$$R_0\left(\vec{r} - \vec{r}_t\right) = R_0(x - x_t, y - y_t) = \sqrt{H^2 + (x - x_t)^2 + (y - y_t)^2} = \sqrt{H^2 + \left|\vec{r} - \vec{r}_t\right|^2}. \tag{8}$$

is a new expression for the distance from the center of the scattered signal-receiving area to the surface with coordinates $\vec{r}$.

Typically, in radar measurement practice, the size of the non-synthesized antenna is much smaller than the range (8), so the components $\frac{(x')^2}{R_0\left(\vec{r} - \vec{r}_t\right)}$ and $\frac{(y')^2}{R_0\left(\vec{r} - \vec{r}_t\right)}$ can be reduced. Considering these simplifications, expression (7) can be represented as follows:

$$R\left(\vec{r}, \vec{r}', \vec{r}_t\right) = R(x, y, x', y', y_t, x_t) = R_0\left(\vec{r} - \vec{r}_t\right) - \frac{(x - x_t)x'}{R_0\left(\vec{r} - \vec{r}_t\right)} - \frac{(y - y_t)y'}{R_0\left(\vec{r} - \vec{r}_t\right)}. \tag{9}$$

The reflection coefficient of electromagnetic waves by the surface $\dot{F}\left(\vec{r}\right)$ is assumed to be a delta-correlated process:

$$\dot{R}_F\left(\vec{r}_1, \vec{r}_2\right) = \left\langle \dot{F}\left(\vec{r}_1\right)\dot{F}\left(\vec{r}_2\right)\right\rangle = \sigma^0\left(\vec{r}_1\right)\delta\left(\vec{r}_1 - \vec{r}_2\right), \tag{10}$$

where $\sigma^0\left(\vec{r}_1\right)$ is the normalized radar cross-section of the area.

2.1.3. Observation Equation

Received signals in the receiver are always observed with internal noise $n\left(t, \vec{r}'\right)$. Then, we use an additive model of the following form to optimize the observation equation.

$$u\left(t, \vec{r}', \vec{r}_t\right) = s_r\left(t, \vec{r}', \vec{r}_t\right) + n\left(t, \vec{r}'\right). \tag{11}$$

2.1.4. Signal and Noise Correlations

The noise in each processing channel is assumed to be mutually uncorrelated. The noise model is described by a Gaussian distribution with the following correlation function:

$$R_n\left(t_1, t_2, \vec{r}_1', \vec{r}_2'\right) = \left\langle n\left(t_1, \vec{r}_1'\right)n\left(t_2, \vec{r}_2'\right)\right\rangle = \frac{N_{0n}}{2}\delta(t_1 - t_2)\delta\left(\vec{r}_1' - \vec{r}_2'\right). \tag{12}$$

The noise energy, i.e., the power spectral density, is assumed to be the same for each receiving channel.

Considering the stochastic nature of the electromagnetic field scattered by the surface, the informative signal's correlation function can be represented by the following equation:

$$\begin{aligned} R_{\mathrm{s}}\left(t_1, t_2, \vec{r_1}', \vec{r_2}', \vec{r}_{\mathrm{t}_1}, \vec{r}_{\mathrm{t}_2}\right) &= \left\langle Re\dot{s}\left(t_1, \vec{r_1}', \vec{r}_{\mathrm{t}_1}\right) Re\dot{s}\left(t_2, \vec{r_2}', \vec{r}_{\mathrm{t}_2}\right)\right\rangle \approx \tfrac{1}{2} Re\left\langle \dot{s}\left(t_1, \vec{r_1}', \vec{r}_{\mathrm{t}_1}\right)\dot{s}^*\left(t_2, \vec{r_2}', \vec{r}_{\mathrm{t}_2}\right)\right\rangle \\ &= \tfrac{1}{2} Re\int_D\int_D \left\langle \dot{F}\left(\vec{r_1}\right)\dot{F}^*\left(\vec{r_2}\right)\right\rangle \dot{s}_0\left(t_1, \vec{r_1}, \vec{r_1}', \vec{r}_{\mathrm{t}_1}\right)\dot{s}_0^*\left(t_2, \vec{r_2}, \vec{r_2}', \vec{r}_{\mathrm{t}_2}\right) d\vec{r_1}\, d\vec{r_2}. \end{aligned} \tag{13}$$

Let us rewrite Equation (13) considering Equation (10):

$$R_{\mathrm{s}}\left(t_1, t_2, \vec{r_1}', \vec{r_2}', \vec{r}_{\mathrm{t}_1}, \vec{r}_{\mathrm{t}_2}\right) = \frac{1}{2} Re\int_D \sigma^0\left(\vec{r}\right)\dot{s}_0\left(t_1, \vec{r}, \vec{r_1}', \vec{r}_{\mathrm{t}_1}\right)\dot{s}_0^*\left(t_2, \vec{r}, \vec{r_2}', \vec{r}_{\mathrm{t}_2}\right) d\vec{r}. \tag{14}$$

The total correlation function of the waves to be further processed, based on the previous equations, is presented as follows:

$$\begin{aligned} R_{\mathrm{u}}\left(t_1, t_2, \vec{r_1}', \vec{r_2}', \vec{r}_{\mathrm{t}_1}, \vec{r}_{\mathrm{t}_2}\right) &= \left\langle u\left(t_1, \vec{r_1}', \vec{r}_{\mathrm{t}_1}\right) u\left(t_2, \vec{r_2}', \vec{r}_{\mathrm{t}_2}\right)\right\rangle \\ &= R_{\mathrm{s}}\left(t_1, t_2, \vec{r_1}', \vec{r_2}', \vec{r}_{\mathrm{t}_1}, \vec{r}_{\mathrm{t}_2}\right) + R_{\mathrm{n}}\left(t_1, t_2, \vec{r_1}', \vec{r_2}'\right) \\ &= \tfrac{1}{2} R\int_D \sigma^0\left(\vec{r}\right)\dot{s}_0\left(t_1, \vec{r}, \vec{r_1}', \vec{r}_{\mathrm{t}_1}\right)\dot{s}_0^*\left(t_2, \vec{r}, \vec{r_2}', \vec{r}_{\mathrm{t}_2}\right) d\vec{r} + \tfrac{N_{0\mathrm{n}}}{2}\delta(t_1 - t_2)\delta\left(\vec{r_1}' - \vec{r_2}'\right). \end{aligned} \tag{15}$$

The primary information about the surface is contained within the parameter known as the power spectral density of the statistically heterogeneous complex radio wave reflection coefficient, $\dot{F}\left(\vec{r}\right)$. This factor is further defined as the radar image of the surface.

2.2. Synthesis of the Optimal Algorithm for Radio Imaging

The optimal restoration of the radar image of the surface, described by the power spectral density of the statistically inhomogeneous complex radio wave reflection coefficient, denoted as $\sigma^0(r)$, must be performed according to the received signals $s_r\left(t, \vec{r}', \vec{r}_{\mathrm{t}}\right)$ in the observation area with coordinates $\vec{r}'$ while the radar sensor moves with the coordinate $\vec{r}_{\mathrm{t}}$, observed in the presence of additive Gaussian noise $n\left(t, \vec{r}'\right)$.

We use the MLE method for the case of the stochastic signals [35] to get the optimal estimation of $\sigma^0(r)$. We modified this function for the case of a static scene observation and possible inspection of the surface along an arbitrary trajectory. Let us denote T as the observation time duration, D' as the area containing all feasible coordinate values within the registration area, and D_{t} as the area containing all potential positions of the system above the observation area. Then, the modified MLE can be presented in the following form:

$$\begin{aligned} &P\left[u\left(t, \vec{r}', \vec{r}_{\mathrm{t}}\right)\Big|\,\sigma^0\left(\vec{r}\right)\right] = \kappa\left[\sigma^0\left(\vec{r}\right)\right] \\ &\times\exp\Big\{-\tfrac{1}{2}\iint_T\iint_{D'}\iint_{D_{\mathrm{t}}} u\left(t_1, \vec{r_1}', \vec{r}_{\mathrm{t}_1}\right) W\left(t_1, t_2, \vec{r_1}', \vec{r_2}', \vec{r}_{\mathrm{t}_1}, \vec{r}_{\mathrm{t}_2}, \sigma^0\left(\vec{r}\right)\right) \\ &\times u\left(t_2, \vec{r_2}', \vec{r}_{\mathrm{t}_2}\right) dt_1\, dt_2\, d\vec{r_1}'\, d\vec{r_2}'\, d\vec{r}_{\mathrm{t}_1}\, d\vec{r}_{\mathrm{t}_2}\Big\}, \end{aligned} \tag{16}$$

where the factor $\kappa\left[\sigma^0\left(\vec{r}\right)\right]$ is characterized by a complex functional dependency on the radio image. Additionally, $W\left(t_1, t_2, \vec{r_1}', \vec{r_2}', \vec{r}_{t_1}, \vec{r}_{t_2}, \sigma^0\left(\vec{r}\right)\right)$ defines the inverse correlation function.

The inverse correlation function is defined through the solution of the integral equation:

$$\int_T \int_{D'} \int_{D_t} R_u\left(t_1, t_2, \vec{r_1}', \vec{r_2}', \vec{r}_{t_1}, \vec{r}_{t_2}, \sigma^0\left(\vec{r}\right)\right) W\left(t_2, t_3, \vec{r_2}', \vec{r_3}', \vec{r}_{t_2}, \vec{r}_{t_3}, \sigma^0\left(\vec{r}\right)\right) d\vec{r}_{t_2}\, d\vec{r_2}'\, dt_2 \\ = \delta(t_1 - t_3)\delta\left(\vec{r_1}' - \vec{r_3}'\right)\delta\left(d\vec{r}_{t_1} - d\vec{r}_{t_3}\right). \tag{17}$$

The MLE using Equation (16) is obtained by calculating the variational derivative and putting it equal to zero. The resulting radar image is expressed as a spatial coordinate function, and the variation $\sigma^0\left(\vec{r}\right)$ is represented as follows:

$$\hat{\sigma}^0\left(\vec{r}\right) = \sigma^0_{\mathrm{opt}}\left(\vec{r}\right) + \delta\sigma^0\left(\vec{r}\right), \tag{18}$$

where $\sigma^0_{\mathrm{opt}}\left(\vec{r}\right)$ is the optimal estimate of the radio image, and $\delta\sigma^0\left(\vec{r}\right)$ is the variation of the radio image estimate, representing some small deviation from the optimally recovered image. The arbitrary function $\delta\sigma^0\left(\vec{r}\right)$ can be written as

$$\delta\sigma^0\left(\vec{r}\right) = \alpha\gamma\left(\vec{r}\right), \tag{19}$$

where $\gamma\left(\vec{r}\right)$ is an arbitrary function of unit amplitude, and α is a small deviation of the variation from the optimal value.

Let us simplify the variational derivative of the function $\delta\sigma^0\left(\vec{r}\right)$ using partial derivatives according to a degree, α. The MLE utilizes an exponential function characterized by a monotonic relationship with its input argument. Thus, taking the derivative of the likelihood function's logarithm instead of the function's derivative will not change its maximum. Taking this into account, we can write as follows:

$$\left.\frac{\delta lnP\left[u\left(t, \vec{r}', \vec{r}_{\mathrm{t}}\right) \,\middle|\, \sigma^0\left(\vec{r}\right)\right]}{\delta\sigma^0\left(\vec{r}\right)}\right|_{\sigma^0(\vec{r}) = \sigma^0_{\mathrm{opt}}(\vec{r})} == \left.\frac{dlnP\left[u\left(t, \vec{r}', \vec{r}_{\mathrm{t}}\right) \,\middle|\, \sigma^0_{\mathrm{opt}}\left(\vec{r}\right) + \alpha\gamma\left(\vec{r}\right)\right]}{d\alpha}\right|_{\alpha=0} = 0, \tag{20}$$

where δ and d are notations for the variational and conventional derivatives.

The result of differentiation (20) can be written as follows:

$$-\iint_T \iint_{D'} \iint_{D_{\mathrm{t}}} \frac{dR_{\mathrm{u}}\left(t_1, t_2, \vec{r_1}', \vec{r_2}', \vec{r}_{\mathrm{t}_1}, \vec{r}_{\mathrm{t}_2}, \sigma^0_{\mathrm{opt}}\left(\vec{r}\right) + \alpha\gamma\left(\vec{r}\right)\right)}{d\alpha} \\ \times W\left(t_2, t_3, \vec{r_2}', \vec{r_3}', \vec{r}_{\mathrm{t}_2}, \vec{r}_{\mathrm{t}_3}, \sigma^0_{\mathrm{opt}}\left(\vec{r}\right) + \alpha\gamma\left(\vec{r}\right)\right) d\vec{r}_{\mathrm{t}_1}\, d\vec{r}_{\mathrm{t}_2}\, d\vec{r_1}'\, d\vec{r_2}'\, dt_1\, dt_2 \\ = \iint_T \iint_{D'} \iint_{D_{\mathrm{t}}} u\left(t_1, \vec{r_1}', \vec{r}_{\mathrm{t}_1}\right) \frac{dW\left(t_2, t_3, \vec{r_2}', \vec{r_3}', \vec{r}_{\mathrm{t}_2}, \vec{r}_{\mathrm{t}_3}, \sigma^0_{\mathrm{opt}}\left(\vec{r}\right) + \alpha\gamma\left(\vec{r}\right)\right)}{d\alpha} \\ \times u\left(t_2, \vec{r_2}', \vec{r}_{\mathrm{t}_2}\right) d\vec{r}_{\mathrm{t}_1}\, d\vec{r}_{\mathrm{t}_2}\, d\vec{r_1}'\, d\vec{r_2}'\, dt_1\, dt_2. \tag{21}$$

Considering the integral Equation (17), we can rewrite (20) in the form:

$$Re \int_{\mathrm{D}} \gamma\left(\vec{r}\right) \Big\{ \tfrac{1}{4} \int_D \sigma^0\left(\vec{r_1}\right) \int_T \int_{D'} \int_{D_{\mathrm{t}}} \dot{s}_0\left(t_1, \vec{r}, \vec{r_1}', \vec{r}_{\mathrm{t}_1}\right) \dot{s}^*_{0\mathrm{W}}\left(t_1, \vec{r_1}, \vec{r_1}', \vec{r}_{\mathrm{t}_1}\right) d\vec{r}_{\mathrm{t}_1}\, d\vec{r_1}'\, dt_1 \\ \times \int_T \int_{D'} \int_{D_{\mathrm{t}}} \dot{s}^*_0\left(t_2, \vec{r}, \vec{r_2}', \vec{r}_{\mathrm{t}_2}\right) \dot{s}_{0\mathrm{W}}\left(t_2, \vec{r_1}, \vec{r_2}', \vec{r}_{\mathrm{t}_2}\right) d\vec{r}_{\mathrm{t}_2}\, d\vec{r_2}'\, dt_2 d\vec{r_1} \\ + \tfrac{1}{2} \tfrac{N_{0\mathrm{n}}}{2} \int_T \int_{D'} \int_{D_{\mathrm{t}}} \dot{s}_{0\mathrm{W}}\left(t_3, \vec{r}, \vec{r_3}', \vec{r}_{\mathrm{t}_3}\right) \dot{s}^*_{0\mathrm{W}}\left(t_3, \vec{r}, \vec{r_3}', \vec{r}_{\mathrm{t}_3}\right) d\vec{r}_{\mathrm{t}_3}\, d\vec{r_3}'\, dt_3 \\ - \tfrac{1}{2} \int_T \int_{D'} \int_{D_{\mathrm{t}}} u\left(t_1, \vec{r_1}', \vec{r}_{\mathrm{t}_1}\right) \dot{s}_{0\mathrm{W}}\left[t_1, \vec{r_1}', \vec{r}_{\mathrm{t}_1}, \sigma^0\left(\vec{r}\right)\right] d\vec{r}_{\mathrm{t}_1}\, d\vec{r_1}'\, dt_1 \\ \times \int_T \int_{D'} \int_{D_{\mathrm{t}}} \dot{s}^*_{0\mathrm{W}}\left[t_2, \vec{r_2}', \vec{r}_{\mathrm{t}_2}, \sigma^0\left(\vec{r}\right)\right] u\left(t_2, \vec{r_2}', \vec{r}_{\mathrm{t}_2}\right) d\vec{r}_{\mathrm{t}_2}\, d\vec{r_2}'\, dt_2 \Big\} d\vec{r} = 0, \tag{22}$$

or

$$Re \int_D \gamma\left(\vec{r}\right) \left\{ \frac{1}{4} \int_D \sigma^0\left(\vec{r_1}\right) \left|\dot{\Psi}_{\mathrm{W}}\left(\vec{r}, \vec{r_1}\right)\right|^2 d\vec{r_1} + \frac{N_{0\mathrm{n}}}{2} \mathcal{E}_{\mathrm{W}}\left(\vec{r}\right) - \frac{1}{2}\left|\dot{Y}\left(\vec{r}\right)\right|^2 \right\} d\vec{r} = 0. \tag{23}$$

where

$$\mathcal{E}_{\mathrm{W}}\left(\vec{r}\right) = \frac{1}{2}\int_T\int_{D'}\int_{D_t}\left|\dot{s}_{0\mathrm{W}}\left(t_3,\vec{r_3}',\vec{r_{t_3}},\sigma^0\left(\vec{r}\right)\right)\right|^2 d\vec{r_{t_3}}\,d\vec{r_3}'\,dt_3. \quad (24)$$

is the energy of the matched signal $\dot{s}_{0\mathrm{W}}\left(t_3,\vec{r_3}',\vec{r_{t_3}},\sigma^0\left(\vec{r}\right)\right)$, considering its decorrelation.

The entire Equation (23) will be equal to zero if the inequality under the integral of the variable $d\vec{r}$ is exactly equal to zero, i.e.:

$$\left|\dot{Y}\left(\vec{r}\right)\right|^2 = \frac{1}{2}\int_D\sigma^0\left(\vec{r_1}\right)\left|\dot{\Psi}_{\mathrm{W}}\left(\vec{r},\vec{r_1}\right)\right|^2 d\vec{r_1} + N_{0\mathrm{n}}\mathcal{E}_{\mathrm{W}}\left(\vec{r}\right). \quad (25)$$

The following equations are used in Equations (22) and (23):

$$\dot{Y}\left(\vec{r}\right) = \int_T\int_{D'}\int_{D_t} u\left(t_1,\vec{r_1}',\vec{r_{t_1}}\right)\dot{s}_{0\mathrm{W}}\left[t_1,\vec{r_1}',\vec{r_{t_1}},\sigma^0\left(\vec{r}\right)\right] d\vec{r_{t_1}}\,d\vec{r_1}'\,dt_1 \quad (26)$$

is the optimal algorithm for processing the received oscillations $u\left(t_1,\vec{r_1}',\vec{r_{t_1}}\right)$ by each element of the antenna array in different spatial positions $\vec{r_{t_1}}$. The processing procedure corresponds to the classical matched filtering in accordance with the observation equation with a reference signal:

$$\dot{s}_{0\mathrm{W}}\left[t_1,\vec{r_1}',\vec{r_{t_1}},\sigma^0\left(\vec{r}\right)\right] = \int_T\int_{D'}\int_{D_t} W\left(t_1,t_3,\vec{r_1}',\vec{r_3}',\vec{r_{t_1}},\vec{r_{t_3}},\sigma^0\left(\vec{r}\right)\right)\dot{s}_0\left(t_3,\vec{r},\vec{r_3}',\vec{r_{t_3}}\right) d\vec{r_{t_3}}\,d\vec{r_3}'\,dt_3. \quad (27)$$

which is previously formed coinciding with the applied geometry. The innovation of the proposed algorithm lies in the novel operation of decorrelating the received oscillations using a filter defined by the impulse response $W\left(t_2,t_3,\vec{r_2}',\vec{r_3}',\vec{r_{t_2}},\vec{r_{t_3}},\sigma^0_{\mathrm{opt}}\left(\vec{r}\right)\right)$. Additionally, it includes a matched filtering of the received signals aligned with the sensor's motion coordinates $\vec{r_{t_1}}$. Further analytical and simulation-based studies are required to evaluate and optimize the selection of efficient 2D trajectory configurations for the radio sensor's movement over stationary ground.

In Equations (22) and (23), the function

$$\dot{\Psi}_{\mathrm{W}}\left(\vec{r},\vec{r_1}\right) = \int_T\int_{D'}\int_{D_t}\dot{s}_0\left(t_1,\vec{r_1},\vec{r_1}',\vec{r_{t_1}}\right)\dot{s}^*_{0\mathrm{W}}\left[t_1,\vec{r_1}',\vec{r_{t_1}},\sigma^0\left(\vec{r_1}\right)\right] d\vec{r_{t_1}}\,d\vec{r_1}'\,dt_1. \quad (28)$$

is the ambiguity function of the radar imaging system, where $\sigma^0\left(\vec{r}\right)$ is the spatial distribution of the normalized radar cross-section, characterizing the system's response to a point radiation source. The ambiguity function in Equation (28) defines the radar system's angular resolution capabilities, which are critical for generating radar images of the surface using static-aperture synthesis technology.

The designed optimal method of radio imaging (26) also can be represented at the level of envelope processing after their detection.

$$\dot{Y}\left(\vec{r}\right) = \frac{1}{2}\int_T\int_{D'}\int_{D_t}\dot{U}\left(t_1,\vec{r_1}',\vec{r_{t_1}}\right)\dot{S}^*_{0\mathrm{W}}\left[t_1,\vec{r_1}',\vec{r_{t_1}},\sigma^0\left(\vec{r}\right)\right] d\vec{r_{t_1}}\,d\vec{r_1}'\,dt_1. \quad (29)$$

The obtained Equations (26) and (29) explain the physical nature of radar imaging in the case of static scenes using a radar sensor placed on a moving platform and scanning along arbitrary trajectories. The processing procedure consists of coherent convolution for the received oscillations at a high frequency $u\left(t_1,\vec{r_1}',\vec{r_{t_1}}\right)$ in Equation (26) or a low frequency $\dot{U}\left(t_1,\vec{r_1}',\vec{r_{t_1}}\right)$ in Equation (29) using a matched filter in the form of a reference signal generated according to the sensing geometry. The difference between the results obtained in this study and the classical theory of finding the maximum of the correlation integral lies in the decorrelation operation for a single signal using the optimal inverse filter $W\left(t_1, t_3, \vec{r}_1{}', \vec{r}_3{}', \vec{r}_{t_1}, \vec{r}_{t_3}, \sigma^0\left(\vec{r}\right)\right)$. As a result of a single signal decorrelation and the following matched filtering, the size of speckles (multiplicative interference) in radar surface images becomes much smaller than with classical processing. Further filtering of such images can enhance the radar resolution. The application of a decorrelation operation gives a super-resolution effect, achieved through the use of an inverse filter described by its impulse response. This approach is commonly used to solve incorrect inverse problems with functions or image reconstruction [36].

2.3. Analysis of the Developed Optimal Algorithm

Let us analyze the algorithm (29) in the case of the absence of a decorrelation procedure.

$$\dot{Y}\left(\vec{r}\right) = \frac{1}{2}\int_T \int_{D'} \int_{D_t} \dot{U}\left(t_1, \vec{r}_1{}', \vec{r}_{t_1}\right) \dot{S}_0^*\left[t_1, \vec{r}, \vec{r}_1{}', \vec{r}_{t_1}\right] d\vec{r}_{t_1}\, d\vec{r}_1{}'\, dt_1, \tag{30}$$

where, considering Equation (9),

$$\begin{aligned} \dot{S}_0^*\left(t_1, \vec{r}, \vec{r}_1{}', \vec{r}_{t_1}\right) &= \dot{I}^*\left(\vec{r}_1{}'\right)\dot{A}^*\left(t - \frac{2R\left(\vec{r}, \vec{r}_1{}', \vec{r}_{t_1}\right)}{c}\right) e^{j2\pi f_0 \frac{2R(\vec{r}, \vec{r}_1{}', \vec{r}_{t_1})}{c}} \\ &\approx \dot{I}^*\left(\vec{r}_1{}'\right) e^{-j2\pi f_0 \frac{2}{c}\frac{(\vec{r}-\vec{r}_{t_1})}{R_0(\vec{r}-\vec{r}_{t_1})}\vec{r}_1{}'} \\ &\quad\times \dot{A}^*\left(t - \frac{2R_0\left(\vec{r}-\vec{r}_{t_1}\right)}{c}\right) e^{j2\pi f_0 \frac{2R_0(\vec{r}-\vec{r}_{t_1})}{c}}, \end{aligned} \tag{31}$$

and $\left(\vec{r} - \vec{r}_{t_1}\right)\vec{r}_1{}' = (x - x_{t_1})x_1' + (y - y_{t_1})y_1'$, which is the scalar product of vectors $\left(\vec{r} - \vec{r}_{t_1}\right)$ and $\vec{r}_1{}'$. We can obtain, substituting (31) into (30), the following equation:

$$\begin{aligned} \dot{Y}\left(\vec{r}\right) &= \tfrac{1}{2}\int_{D_t}\int_T \left[\int_{D'} \dot{U}\left(t_1, \vec{r}_1{}', \vec{r}_{t_1}\right)\dot{I}^*\left(\vec{r}_1{}'\right) e^{-j2\pi f_0 \frac{2}{c}\frac{(\vec{r}-\vec{r}_{t_1})}{R_0(\vec{r}-\vec{r}_{t_1})}\vec{r}_1{}'} d\vec{r}_1{}'\right] \\ &\quad\times \dot{A}^*\left(t - \frac{2R_0\left(\vec{r}-\vec{r}_{t_1}\right)}{c}\right) dt_1\, e^{j2\pi f_0 \frac{2R_0(\vec{r}-\vec{r}_{t_1})}{c}} d\vec{r}_{t_1} \\ &= \tfrac{1}{2}\int_{D_t}\left[\int_T \dot{U}_{\mathrm{I}}\left(t_1, \vec{r}, \vec{r}_{t_1}\right)\dot{A}^*\left(t - \frac{2R_0\left(\vec{r}-\vec{r}_{t_1}\right)}{c}\right) dt_1\right] e^{j2\pi f_0 \frac{2R_0(\vec{r}-\vec{r}_{t_1})}{c}} d\vec{r}_{t_1}. \end{aligned} \tag{32}$$

According to (32), the processing procedure's essence can be explained as follows. A scanner with a radio sensor receives signals along a predefined trajectory in the $\vec{r}_t$ coordinates. The recorded oscillations at each antenna array element are processed using the weighting coefficients in the complex–conjugate amplitude–phase distribution, denoted as $\dot{I}^*\left(\vec{r}_1{}'\right)$. Following the amplification phase, the signals at each array element are aligned to a common phase center by applying the phase shift factor $e^{-j2\pi f_0 \frac{2}{c}\frac{(\vec{r}-\vec{r}_{t_1})}{R_0(\vec{r}-\vec{r}_{t_1})}\vec{r}_1{}'}$. A multi-beam radiation pattern is formed by averaging the phased signals, with the antenna array constantly focused on each surface point $\vec{r}$ when the sensor changes along the $\vec{r}_{t_1}$ coordinates. After the signal processing in the antenna array, the oscillations undergo time matching for subsequent processing. The form of the complex envelope is $\dot{A}^*\left(t - \frac{2R_0\left(\vec{r}-\vec{r}_{t_1}\right)}{c}\right)$. Then, the time processing can be any-pulse, continuous, without or with intra-pulse modulation. The critical aspect of time processing is the precise amplitude and phase-matched detection of the received signals. This detection is performed at the level of detected amplitudes, which are known as a trajectory signal when accumulated during the spatial scanning process. These detected amplitudes are then processed through a filter described by the following impulse response during the radio image synthesis phase:

$$e^{j2\pi f_0 \frac{2\sqrt{H^2+|\vec{r}-\vec{r}_{t_1}|^2}}{c}}. \tag{33}$$

When the detection results are digitized and processed computationally, generating a reference signal with a square root in the argument of the e function poses no significant challenge. However, suppose the processing is carried out directly within a radio system hardware. In that case, expressing the resulting function (33) as a basis function associated with well-established Fresnel or Fourier transforms is more practical. Let us simplify the function (33) by expanding the root

$$\sqrt{H^2+\left|\vec{r}-\vec{r}_{t_1}\right|^2} = H\sqrt{1+\frac{\left|\vec{r}-\vec{r}_{t_1}\right|^2}{H^2}}, \tag{34}$$

in the Taylor series under condition $\frac{\left|\vec{r}-\vec{r}_{t_1}\right|^2}{H^2} \leq 1$, obtaining

$$H\left(1+\frac{1}{2}\frac{\left|\vec{r}-\vec{r}_{t_1}\right|^2}{H^2}\right) = H+\frac{(x-x_{t_1})^2+(y-y_{t_1})^2}{2H} = H+\frac{(x-x_{t_1})^2}{2H}+\frac{(y-y_{t_1})^2}{2H}. \tag{35}$$

Substituting Equation (35) into Equation (32), we write the processing procedure as follows:

$$\begin{aligned}\dot{Y}\left(\vec{r}\right) = \exp\left\{j2\pi f_0 \tfrac{2H}{c}\right\} \tfrac{1}{2}\int_{D_{yt}}\int_{D_{xt}}&\left[\int_T \dot{U}_{\mathrm{I}}\left(t_1,\vec{r},\vec{r}_{t_1}\right)\dot{A}^*\left(t-\frac{2R_0\left(\vec{r}-\vec{r}_{t_1}\right)}{c}\right)dt_1\right] \\ &\times e^{j2\pi f_0 \frac{(x-x_{t_1})^2}{cH}} e^{j2\pi f_0 \frac{(y-y_{t_1})^2}{cH}}\, dx_{t_1}\, dy_{t_1}.\end{aligned} \tag{36}$$

According to Equation (25), once the optimal output effect in Equation (36) has been formed, the computation of its squared modulus is required. Since the squared modulus of $e^{j2\pi f_0 \frac{2H}{c}}$ equals one, this step can be omitted in the formation of $\dot{Y}\left(\vec{r}\right)$. In general, the spatial coordinate (x_{t1}, y_{t1}) processing involves performing operations akin to the general inverse spatial Fresnel transform. Through these optimal processing steps, the aperture of the radio system's antenna array D is synthesized to the dimensions of the scanning area D_t. The synthesis quality is impacted by the trajectory of the radio sensor along the spatial coordinates (x_{t1}, y_{t1}). The spatial resolution of radar for surface radio imaging using the static-aperture synthesis technique will be analyzed by defining the ambiguity function and demonstrated through results from simulation modeling.

2.4. System's Ambiguity Function Without the Reference Signal Decorrelation

We can represent the modulus square of the function (28), considering Equations (3), (9) and (35) in such form:

$$
\begin{aligned}
\left|\dot{\Psi}\left(\vec{r},\vec{r_1}\right)\right|^2 &= \left|\int_T \int_{D'} \int_{D_t} \dot{I}\left(\vec{r_1}'\right)\dot{A}\left(t_1-\frac{2R_0\left(\vec{r}-\vec{r_{t_1}}\right)}{c}\right)e^{j2\pi f_0 t_1}e^{-j2\pi f_0\frac{2H}{c}}e^{-j2\pi f_0\frac{|\vec{r}-\vec{r_{t_1}}|^2}{cH}}\right.\\
&\quad\times e^{j2\pi f_0\frac{2}{c}\frac{\vec{r}-\vec{r_{t_1}}}{R_0(\vec{r}-\vec{r_{t_1}})}\vec{r_1}'}\dot{I}^*\left(\vec{r_1}'\right)\dot{A}^*\left(t_1-\frac{2R_0\left(\vec{r_1}-\vec{r_{t_1}}\right)}{c}\right)e^{-j2\pi f_0 t_1}e^{j2\pi f_0\frac{2H}{c}}\\
&\quad\left.\times e^{j2\pi f_0\frac{|\vec{r_1}-\vec{r_{t_1}}|^2}{cH}}e^{-j2\pi f_0\frac{2}{c}\frac{\vec{r_1}-\vec{r_{t_1}}}{R_0(\vec{r}-\vec{r_{t_1}})}\cdot\vec{r_1}'}d\vec{r_{t_1}}\,d\vec{r_1}'\,dt_1\right|^2\\
&= \left|\int_{D_t}\int_{D'}\left|\dot{I}\left(\vec{r_1}'\right)\right|^2 e^{j2\pi f_0\frac{2}{c}\frac{\vec{r}-\vec{r_{t_1}}}{R_0(\vec{r}-\vec{r_{t_1}})}\vec{r_1}'}e^{-j2\pi f_0\frac{2}{c}\frac{\vec{r_1}-\vec{r_{t_1}}}{R_0(\vec{r}-\vec{r_{t_1}})}\vec{r_1}'}d\vec{r_1}'\right.\\
&\quad\left.\times\int_T \dot{A}\left(t_1-\frac{2R_0\left(\vec{r}-\vec{r_{t_1}}\right)}{c}\right)\dot{A}^*\left(t_1-\frac{2R_0\left(\vec{r_1}-\vec{r_{t_1}}\right)}{c}\right)dt_1 e^{-j2\pi f_0\frac{|\vec{r}-\vec{r_{t_1}}|^2}{cH}}e^{j2\pi f_0\frac{|\vec{r_1}-\vec{r_{t_1}}|^2}{cH}}d\vec{r_{t_1}}\right|^2\\
&= \left|R_A\left(\vec{r},\vec{r_1}\right)\dot{\Psi}_{\dot{I}}\left(\vec{r}-\vec{r_1}\right)\int_{D_t}e^{-j2\pi f_0\frac{|\vec{r}-\vec{r_{t_1}}|^2}{cH}}e^{j2\pi f_0\frac{|\vec{r_1}-\vec{r_{t_1}}|^2}{cH}}d\vec{r_{t_1}}\right|^2,
\end{aligned}
\tag{37}
$$

where

$$
R_A\left(\vec{r},\vec{r_1}\right) = \int_T \dot{A}\left(t_1-\frac{2R_0\left(\vec{r}-\vec{r_{t_1}}\right)}{c}\right)\dot{A}^*\left(t_1-\frac{2R_0\left(\vec{r_1}-\vec{r_{t_1}}\right)}{c}\right)dt_1 \tag{38}
$$

is the autocorrelation function of the sensing signal complex envelope, and

$$
\dot{\Psi}_{\dot{I}}\left(\vec{r}-\vec{r_1}\right) = \int_{D'}\left|\dot{I}\left(\vec{r_1}'\right)\right|^2 e^{j2\pi f_0\frac{2}{c}\frac{\vec{r}-\vec{r_1}}{R_0(\vec{r}-\vec{r_{t_1}})}\vec{r_1}'}d\vec{r_1}' \tag{39}
$$

is the convolution of the antenna array's complex radiation pattern.

As observed in Appendix A.2, the integral under the modulus sign in Equation (37), when considering scanning across all possible coordinates within the rectangular area D_t, can be denoted as:

$$
\begin{aligned}
&\int_{D_{xt}}\int_{D_{yt}} e^{-j2\pi f_0\frac{(x-x_{t_1})^2}{cH}}e^{-j2\pi f_0\frac{(y-y_{t_1})^2}{cH}}e^{j2\pi f_0\frac{(x_1-x_{t_1})^2}{cH}}e^{j2\pi f_0\frac{(y_1-y_{t_1})^2}{cH}}dx_{t_1}\,dy_{t_1}\\
&\quad= \int_{-\frac{D_{xt}}{2}}^{\frac{D_{xt}}{2}} e^{-j2\pi f_0\frac{(x-x_{t_1})^2}{cH}}\\
&\quad\times e^{j2\pi f_0\frac{(x_1-x_{t_1})^2}{cH}}dx_{t_1}\int_{-\frac{D_{yt}}{2}}^{\frac{D_{yt}}{2}} e^{-j2\pi f_0\frac{(y-y_{t_1})^2}{cH}}e^{j2\pi f_0\frac{(y_1-y_{t_1})^2}{cH}}dy_{t_1}\\
&= e^{-j2\pi f_0\frac{x^2-x_1^2}{cH}}e^{-j2\pi f_0\frac{y^2-y_1^2}{cH}}D_{xt}\sin c\left(2\pi f_0\frac{x-x_1}{cH}D_{xt}\right)D_{yt}\sin c\left(2\pi f_0\frac{y-y_1}{cH}D_{yt}\right).
\end{aligned}
\tag{40}
$$

Substituting (40) into (37), we obtain

$$
\begin{aligned}
&\left|\dot{\Psi}\left(\vec{r},\vec{r_1}\right)\right|^2 = \left|\dot{\Psi}(x,y,x_1,y_1)\right|^2\\
&= |R_A(x,y,x_1,y_1)\dot{\Psi}_{\dot{I}}(x-x_1,y-y_1)e^{-j2\pi f_0\frac{x^2-x_1^2}{cH}}e^{-j2\pi f_0\frac{y^2-y_1^2}{cH}}\\
&\quad\times D_{xt}\sin c\left(2\pi f_0\frac{x-x_1}{cH}D_{xt}\right)D_{yt}\sin c\left(2\pi f_0\frac{y-y_1}{cH}D_{yt}\right)\Big|^2\\
&= \left|R_A(x,y,x_1,y_1)\dot{\Psi}_{\dot{I}}(x-x_1,y-y_1)D_{xt}\sin c\left(2\pi f_0\frac{x-x_1}{cH}D_{xt}\right)D_{yt}\sin c\left(2\pi f_0\frac{y-y_1}{cH}D_{yt}\right)\right|^2.
\end{aligned}
\tag{41}
$$

So, in such systems, the width of the ambiguity function is defined by the autocorrelation properties of the signals, the convolution of the antenna array far-field patterns, and the $\sin c(\cdot)$ function, whose width is inversely proportional to the scanner's motion area D_t. The analysis of Equation (41) highlights that a distinctive feature of the proposed method is its capacity to achieve high resolution without requiring modulation of the sensing signal. For instance, when a continuous signal is used, the function R_{A} remains nearly constant, offering no resolution in spatial coordinates. In such cases, the width of the $\dot{\Psi}(x - x_1, y - y_1)$ function is inversely related to the dimensions of the radio system's antenna array and is usually much wider than the function $D_{\mathrm{xt}} \sin\mathrm{c}\left(2\pi f_0 \frac{x-x_1}{cH} D_{\mathrm{xt}}\right) D_{\mathrm{yt}} \sin\mathrm{c}\left(2\pi f_0 \frac{y-y_1}{cH} D_{\mathrm{yt}}\right)$. Thus, we obtain a high-resolution estimation of $\sigma^0\left(\vec{r}\right)$ by implementing only coherent processing along the $\vec{r}_{\mathrm{t}}$ coordinates.

A point worth mentioning is that this case of ambiguity function evaluation is only a specific case. Other, potentially faster trajectories for achieving high-precision radar imaging remain to be explored in future research.

2.5. Radar Radio Imaging with the Static-Aperture Synthesis Technique

Consider the basic signal processing operations according to Equation (26). The oscillations $u\left(t, \vec{r}', \vec{r}_{\mathrm{t}}\right)$ received by each antenna element located at coordinates $\vec{r}'$ over the time interval T, as the sensor moves along a specified trajectory coordinates $\vec{r}_{\mathrm{t}}$, should be first processed via the antenna-applied weight averaging with an amplitude–phase distribution $\dot{I}\left(\vec{r}'\right)$. Following this initial processing, the signals are shifted to an intermediate frequency and subjected to a matched filtering in the receivers using a complex amplitude $\dot{A}(t)$. Moreover, in order to enhance the informational content of the signals, the envelopes resulting from the matched filtering are passed through a decorrelation filter, where the degree of decorrelation is proportional to the pre-determined normalized radar cross-section of the surface. The primary operation of the static-aperture synthesis entails performing the matched filtering of the signal envelopes using the trajectory signal accumulated during the movement of the radio sensor along $\vec{r}_{\mathrm{t}}$. This matched filtering is performed as a convolution between the received oscillations and reference signals. Through matched filtering along the sensor trajectory, a high-resolution radar image is reconstructed, impacted by the cross-section of the ambiguity function $\dot{\Psi}_W\left(\vec{r}, \vec{r}_1\right)$. All these operations can be seen in a block diagram (Figure 2).

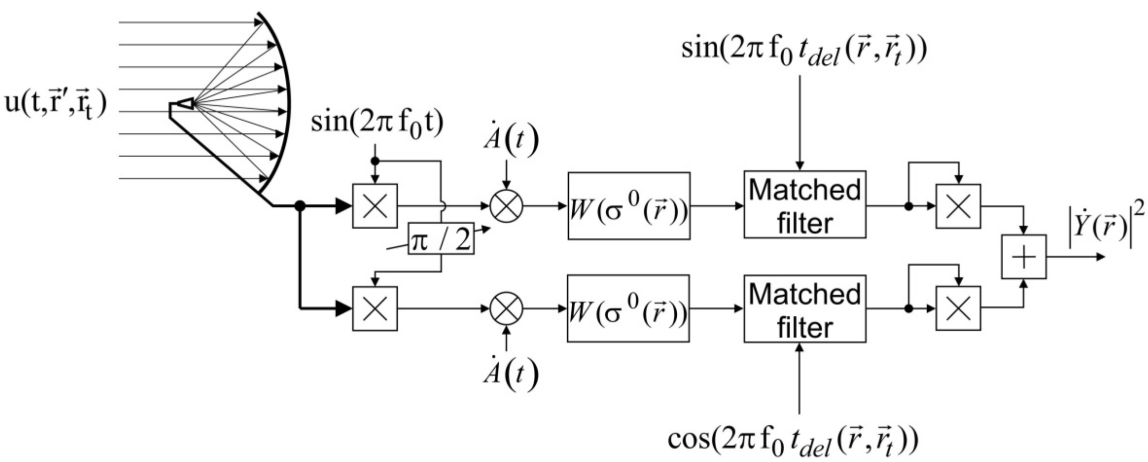

Figure 2. Block diagram of the radar for radio imaging of surfaces with the static-aperture synthesis technique.

2.6. Modeling of Radio Imaging of Surfaces by Systems with Static-Aperture Synthesis

Equation (25) describes the principal processing operations in the radar with the static-aperture synthesis technique. The right side of this equation represents the physical output effect that should be obtained from signal processing. This processing effect can be expressed as the sum of two components. The first is the convolution of the actual radar image with the squared modulus of the ambiguity function, while the second represents the cumulative energy of the received signals with noise. In the absence of a decorrelation operation, the second component remains constant. A simulation model for radar image construction was developed based on the first component, and its structure is shown as the block diagram of key mathematical operations in Figure 3.

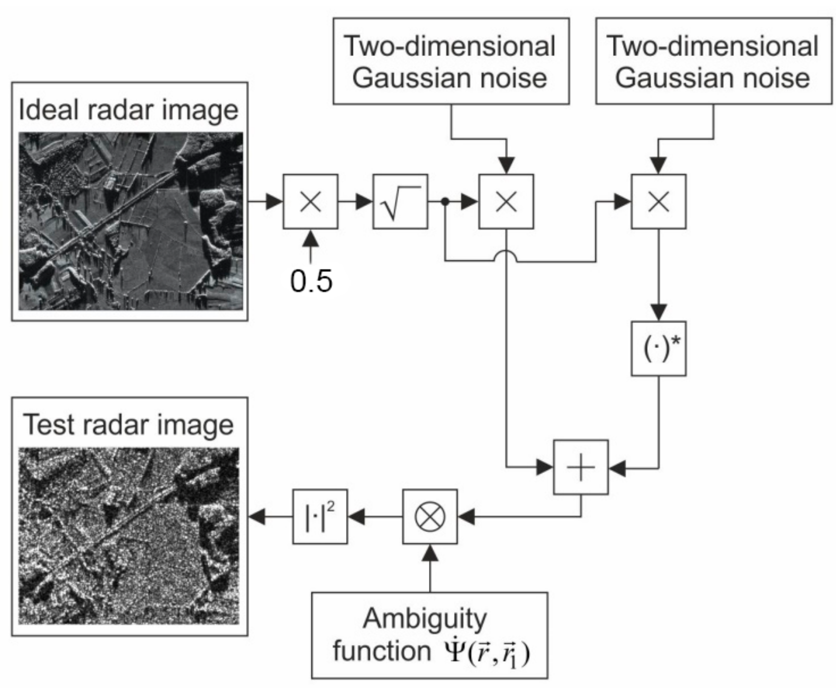

Figure 3. Block diagram of the radar imaging in the simulation model.

The diagram presented in Figure 3 includes the following components: the *ideal radar image*, representing a pre-stored "ideal" high-resolution radar image; *two-dimensional Gaussian noise* units, used to produce spatially discrete Gaussian noise with unit variance; operation blocks, labeled, such as $+$, $\times$, $\sqrt{}$, $(\cdot)^*$ and $|\cdot|^2$, which correspondingly represent a symbol of the addition, the product, the square root operation, the complex conjugation and the modulus square calculation operations; the *ambiguity function* $\dot{\Psi}\left(\vec{r},\vec{r}_1\right)$, which is a previously generated two-dimensional ambiguity function, and the *test radar image* being the resulting test radar image of the simulation modeling.

3. Results and Discussion

This section presents the outputs of the simulation model presented in the previous section and discusses the results to find the key insights. The experimental setup is described below.

A series of test ambiguity functions was employed in the simulation model illustrated in Figure 3. The series was generated by varying the carrier trajectories, which corresponds to modifying $\vec{r}_{t_1}$ in expression (37). The initial parameters for the simulation were set as follows: the maximum dimensions of the carrier trajectory area $D_{x_t} = 0.5$ m and $D_{y_t} = 0.5$ m, height $H = 0.25$ m, and signal frequency $f_0 = 3$ GHz.

Figures 4–13 show the motion trajectories within a rectangular study area and the ambiguity functions $\left|\dot{\Psi}(\Delta x, \Delta y)\right|^2$ for scenarios involving the observation of a point source. The ambiguity function values for different sensing trajectories are obtained according to Equation (41), assuming a continuous sensing signal followed by normalization.

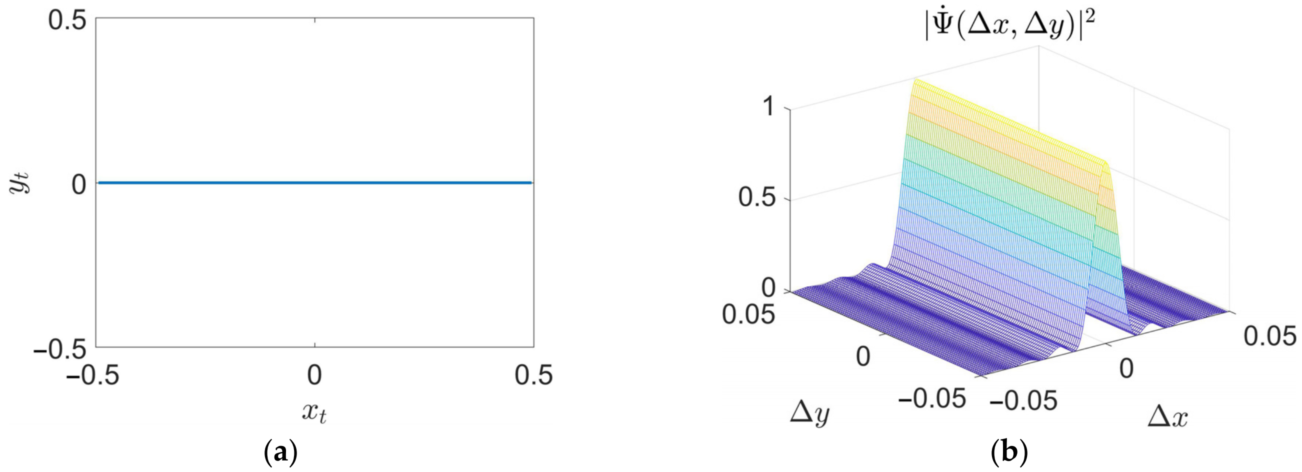

Figure 4. Scanner trajectory (**a**) and the corresponding ambiguity function (**b**) for linear motion along the x-coordinate.

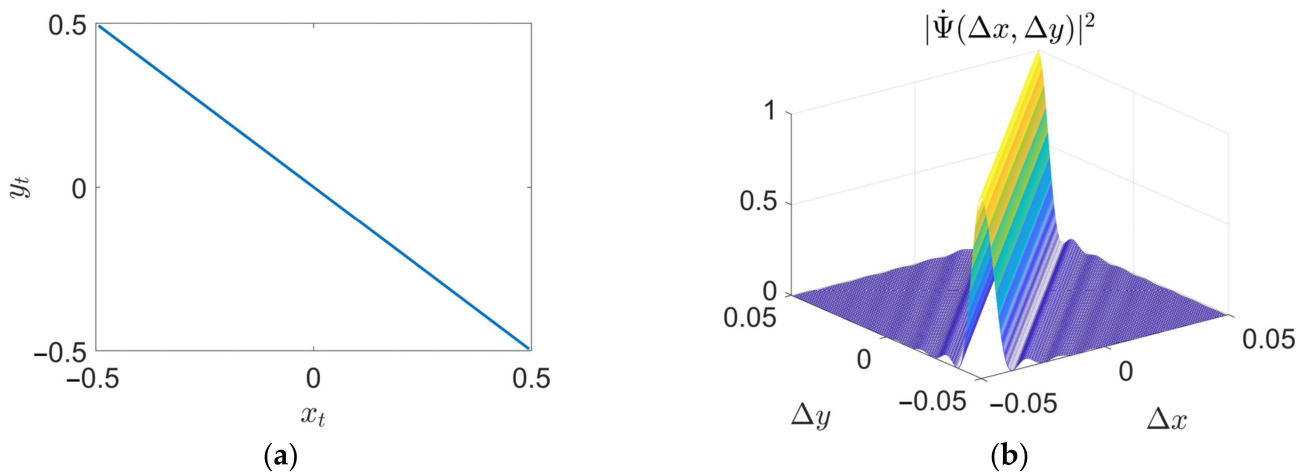

Figure 5. Scanner trajectory (**a**) and corresponding ambiguity function (**b**) for linear diagonal motion.

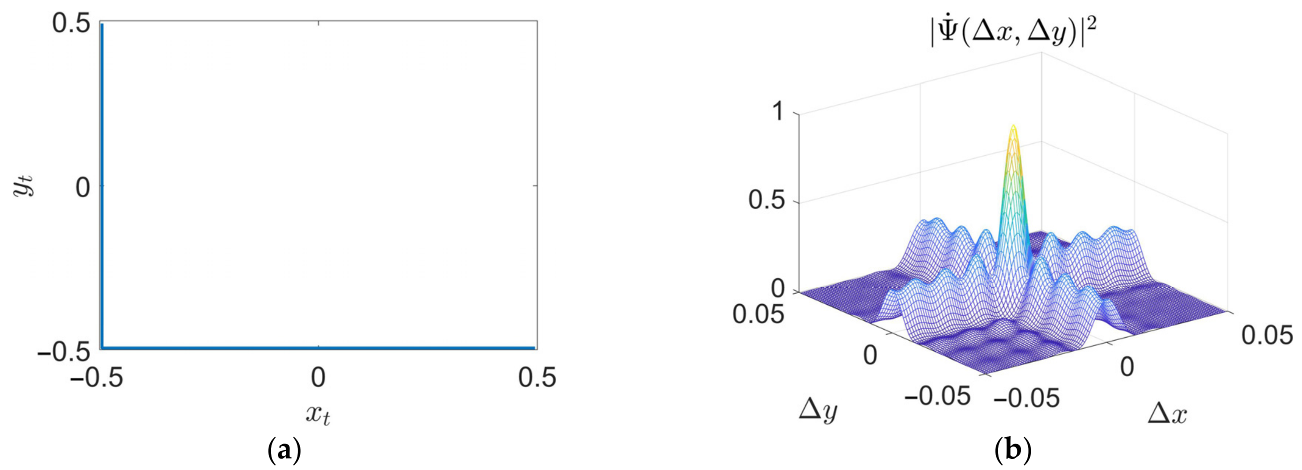

Figure 6. Scanner trajectory (**a**) and the corresponding ambiguity function (**b**) for L-shaped motion.

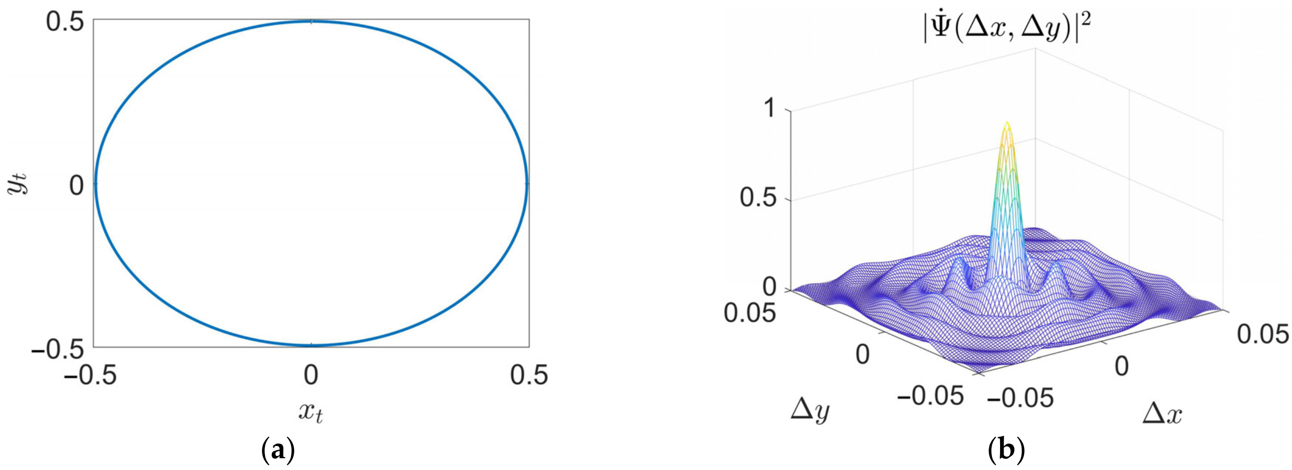

Figure 7. Scanner trajectory (**a**) and corresponding ambiguity function (**b**) for circular motion.

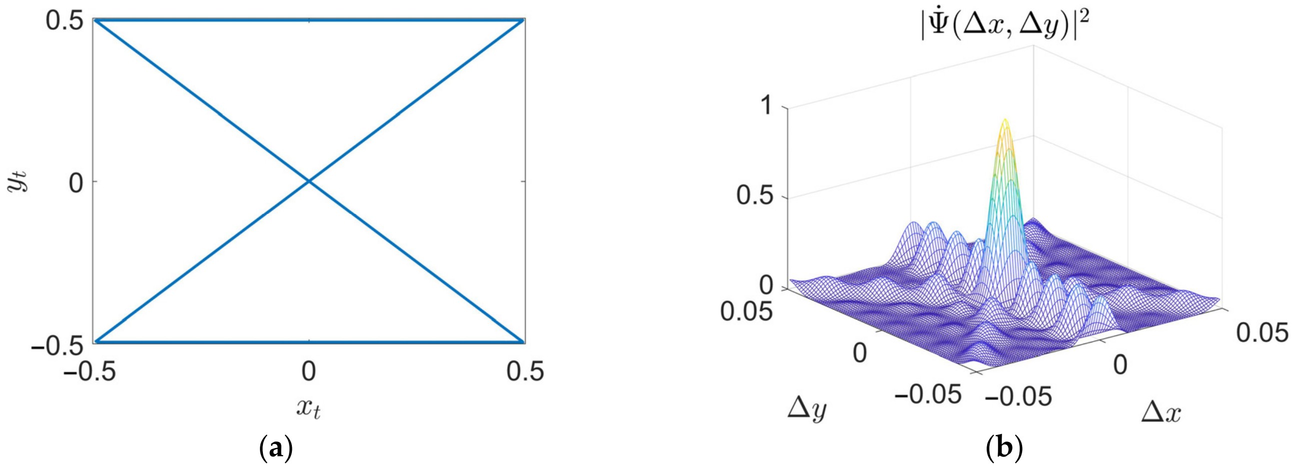

Figure 8. Scanner trajectory (**a**) and corresponding ambiguity function (**b**) for an hourglass-shape motion.

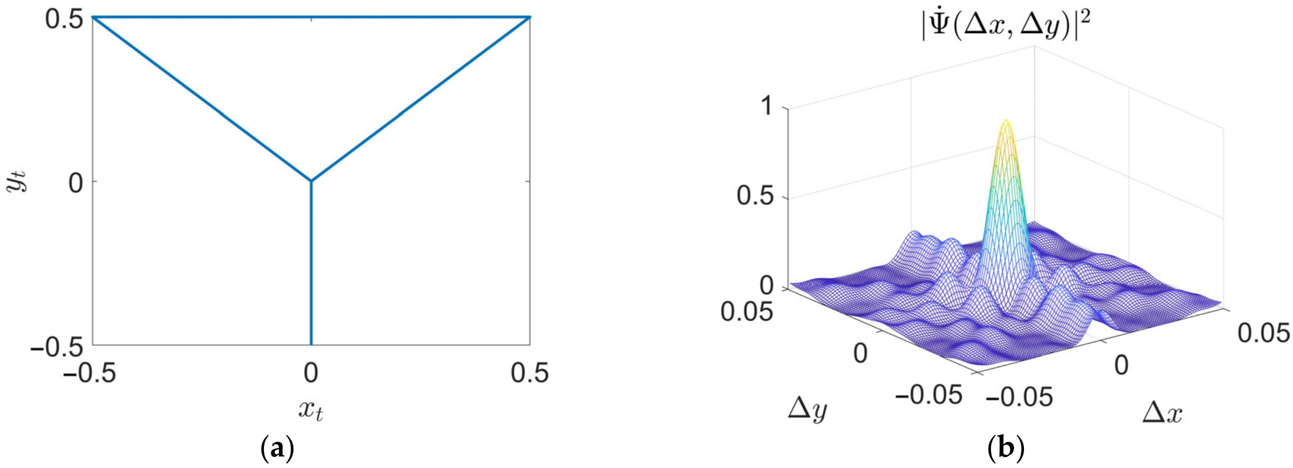

Figure 9. Scanner trajectory (**a**) and corresponding ambiguity function (**b**) for a Y-shaped motion.

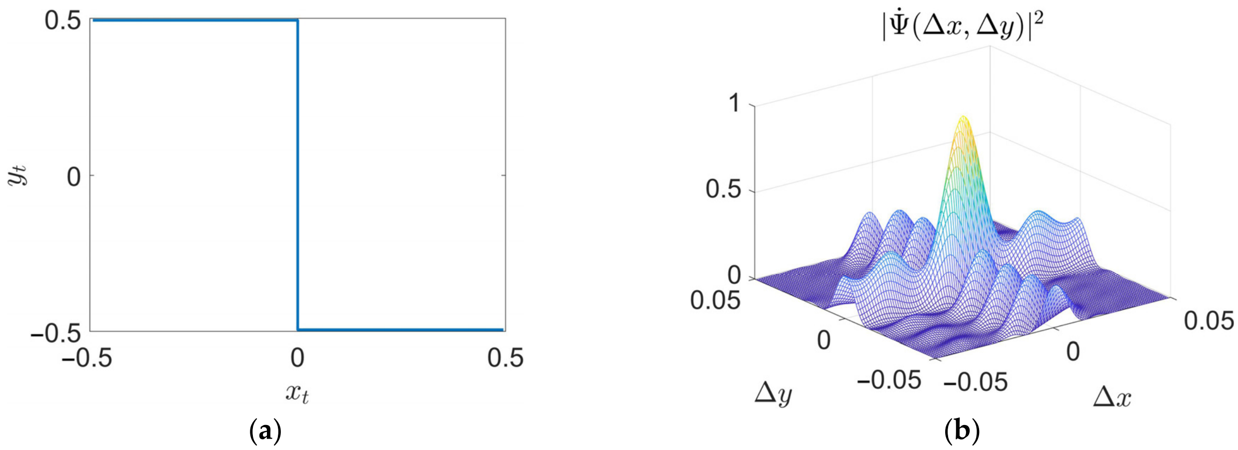

Figure 10. Scanner trajectory (**a**) and corresponding ambiguity function (**b**) for Z-shaped motion.

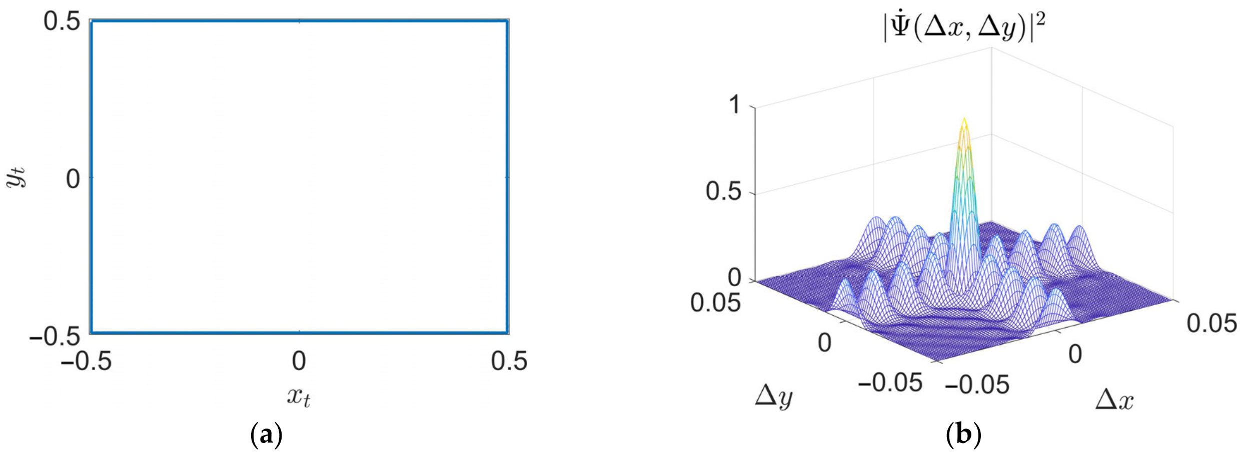

Figure 11. Scanner trajectory (**a**) and corresponding uncertainty function (**b**) for a square motion.

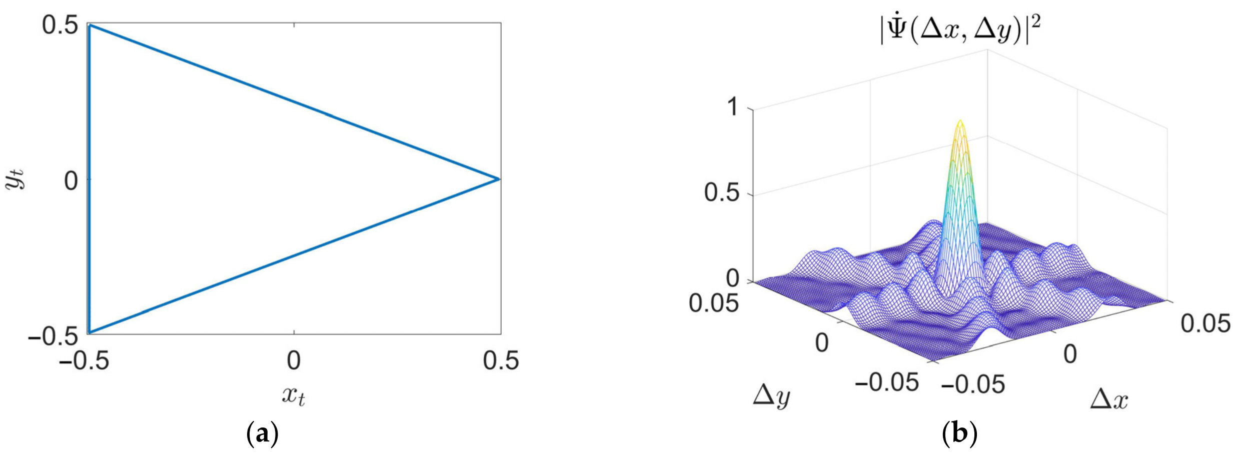

Figure 12. Scanner trajectory (**a**) and corresponding ambiguity function (**b**) for an "isosceles triangle" motion.

The ambiguity functions obtained from the model presented in Figures 4–13 were used to generate the radar images (Figure 14b–k). The ideal (true) radar image [37] is shown in Figure 14a.

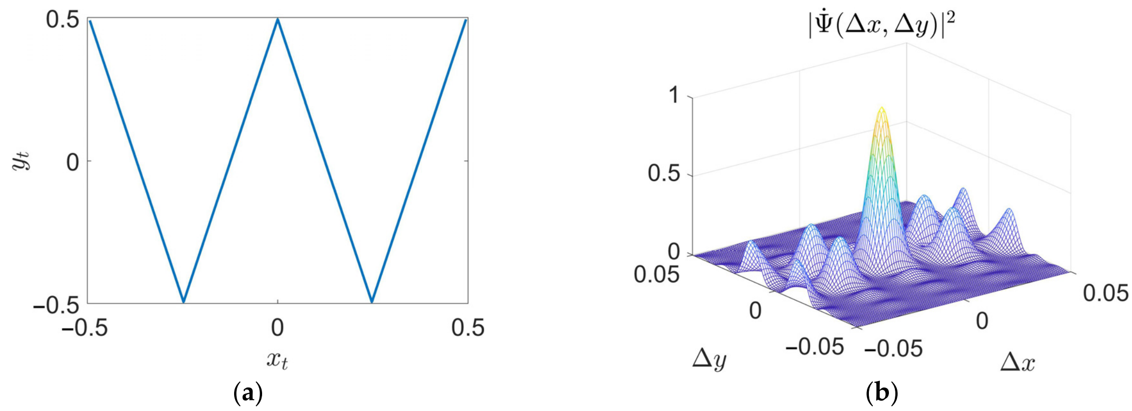

Figure 13. Scanner trajectory (**a**) and corresponding ambiguity function (**b**) for a W-shaped motion.

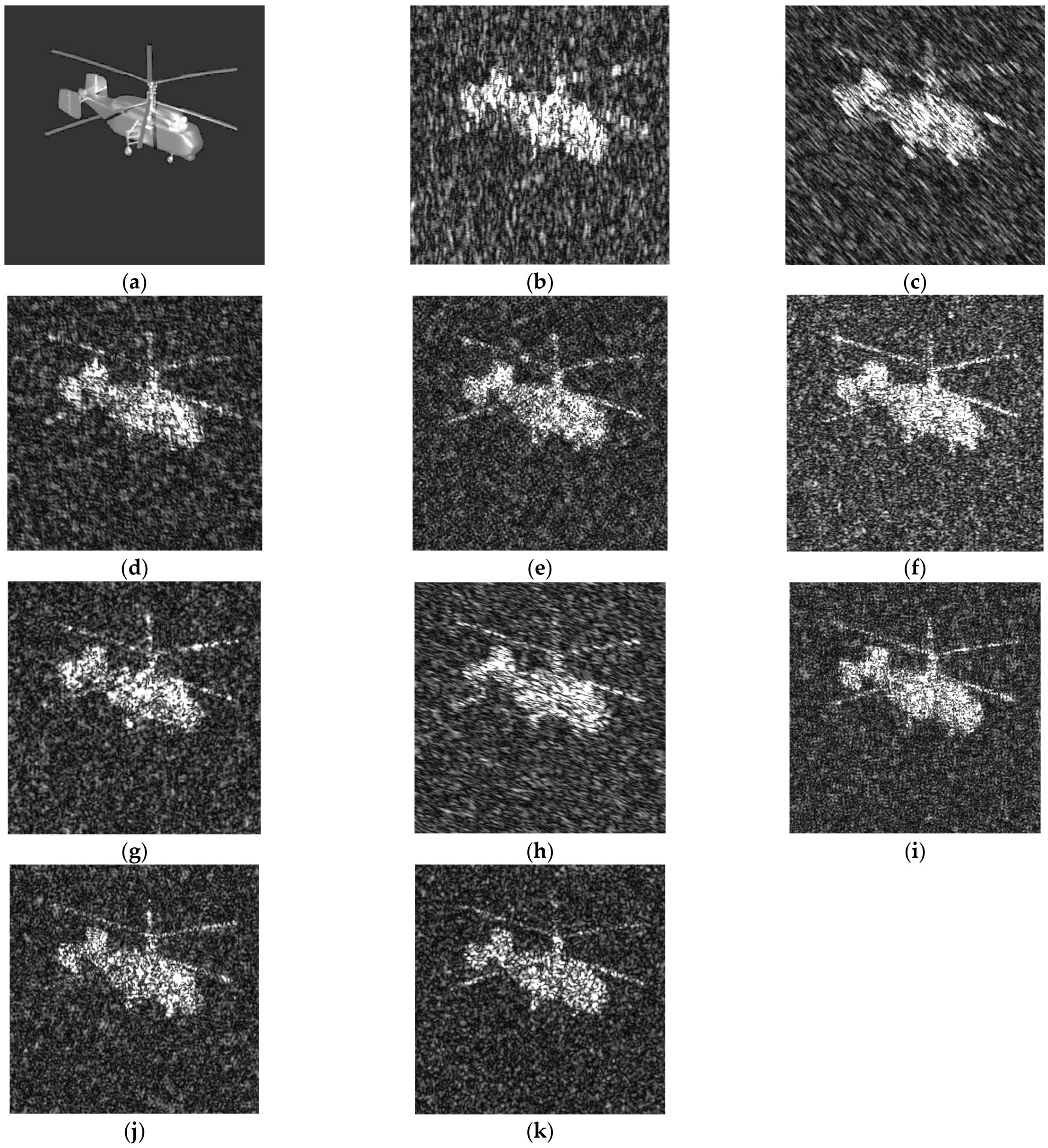

Figure 14. Ideal radar image (**a**) and radar images obtained for the following motion trajectories: (**b**) linear motion along the x-coordinate; (**c**) linear diagonal motion; (**d**) L-shaped motion, (**e**) circular motion; (**f**) hourglass-shape motion; (**g**) Y-shaped motion; (**h**) Z-shaped motion; (**i**) square motion; (**j**) "isosceles triangle" motion; (**k**) W-shaped motion.

Analyzing the results of the proposed model can be effectively achieved by comparing the difference between an ideal radar image and a series of images generated using various ambiguity functions. For this purpose, the following benchmark metrics were chosen: mean square error (MSE), peak signal-to-noise ratio (PSNR), and the structural similarity index measure (SSIM). A point worth mentioning is that these metrics were employed to evaluate 500 estimations for each motion trajectory. The average results are shown in Table 1.

Table 1. Average results of the radar image recovery in accordance with criteria MSE, PSNR, and SSIM. The best results for each criterion are highlighted in bold.

Figure	Motion Trajectory	MSE	PSNR	SSIM
Figure 14a	-	0	Inf	1
Figure 14b	Linear along x-coordinate	0.0368	14.387	0.2093
Figure 14c	Linear diagonal motion	0.0365	14.575	0.2434
Figure 14d	L-shaped motion	0.0322	15.131	0.2422
Figure 14e	Circular motion	0.0292	15.545	0.2179
Figure 14f	Hourglass-shape motion	0.0277	15.723	0.2247
Figure 14g	Y-shaped motion	0.0308	15.324	**0.2796**
Figure 14h	Z-shaped motion	0.0345	14.864	0.2457
Figure 14i	Square motion	**0.0263**	**15.991**	0.1992
Figure 14j	"Isosceles triangle" motion	0.0288	15.579	0.2479
Figure 14k	W-shaped motion	0.0295	15.502	0.2718

Based on the simulation results, the best radio scanner trajectories among the presented ones can be considered the square trajectory (the best performance according to MSE and PSNR values) and the Y-shaped trajectory (the best performance according to the SSIM measure). Instead, the worst of the proposed ones can be considered a linear motion along the x-coordinate, which, in a sense, reflects the classical synthesis of the aperture typical for a side-looking SAR system.

If we compare the results for the trajectories shown in Figure 14b,i, we can see that changing the trajectory from the radio scanner's linear movement along the x-coordinate to the square trajectory will improve the image recovery's PSNR by up to 12%.

It is advisable to study cases when the motion trajectory is not ideal, as this is always the case in practice, because each positioning system has its own spatial coordinate change step and displacement. To investigate this effect, we selected the square trajectory, which was found to be the best for ideal movement, and added some variation to this geometry. The resulting trajectories with 2.5 mm, 5 mm, and 7.5 mm variations are shown in Figure 15a,c,e, respectively. For each of these trajectories, ambiguity functions $|\dot{\Psi}(\Delta x, \Delta y)|^2$ were obtained for the cases of observing a point source (Figure 15b,d,f, respectively).

It can be argued with a visual comparison of the ambiguity function for the idealized trajectory (see Figure 11b) with the obtained ambiguity functions in Figure 15 that, at a variation of 2.5 mm (Figure 15b), the level of the side lobes of the ambiguity function of the system increases; at a variation of 5 mm (Figure 15d), the level of the side lobes begins to change abruptly, and their width value changes; and at a variation of 7.5 mm (Figure 15f) the effects of the curvature of the side lobes become more distinct as some amplitudes increase and the plane becomes heterogeneous.

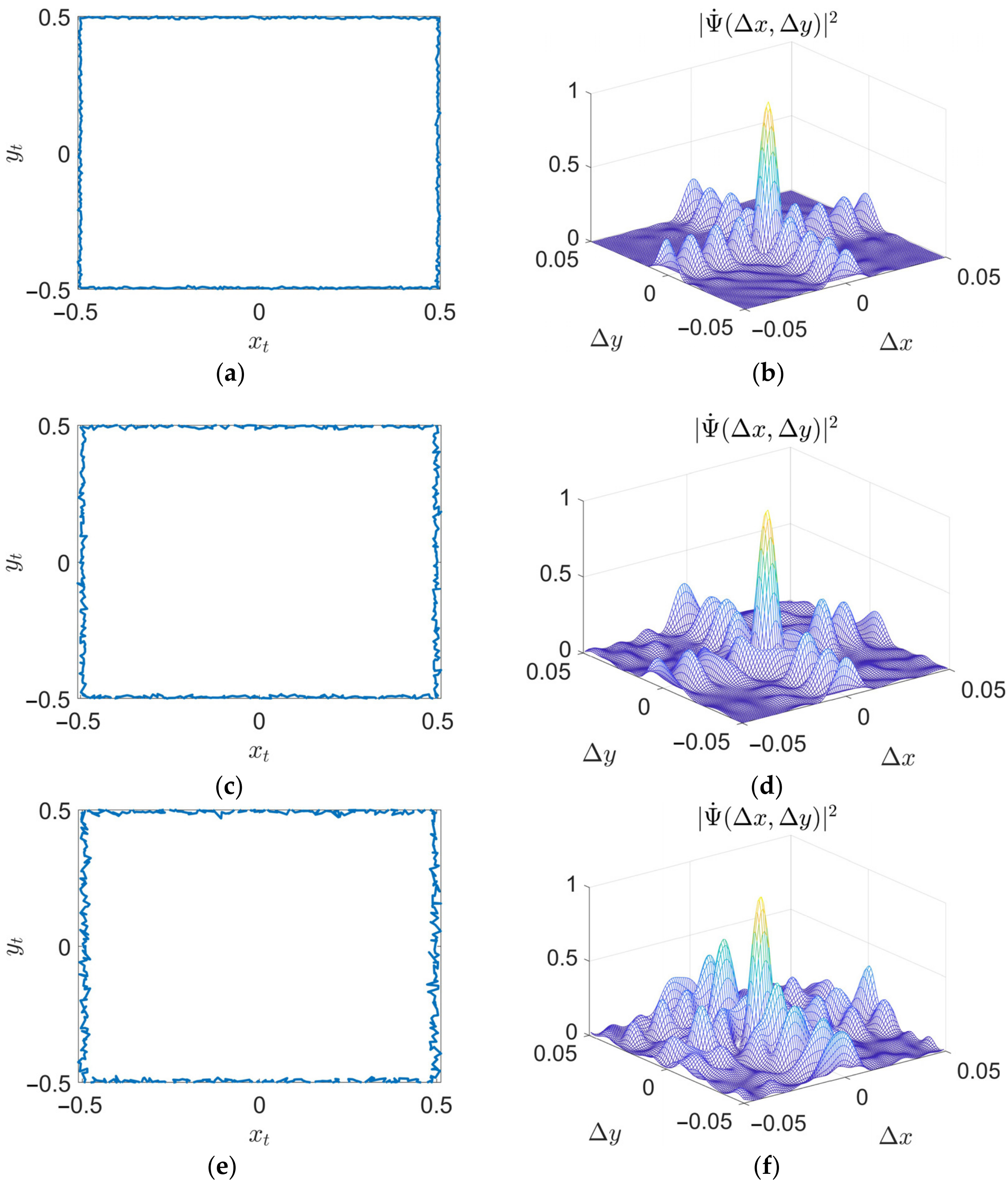

Figure 15. Scanner trajectories and corresponding ambiguity functions for a square motion with (**a**,**b**) 2.5 mm variation; (**c**,**d**) 5 mm variation; (**e**,**f**) 7.5 mm variation.

Figure 16 shows the obtained radar images for the studied trajectories with the variations presented in Figure 15. If we visually compare the obtained radar image for the ideal trajectory with the restored radar images, the following conclusion can be stated: As the trajectory variation grows, the appearance of more high-intensity spots increases, which can lead to incorrect interpretations of the presence of additional objects in the image.

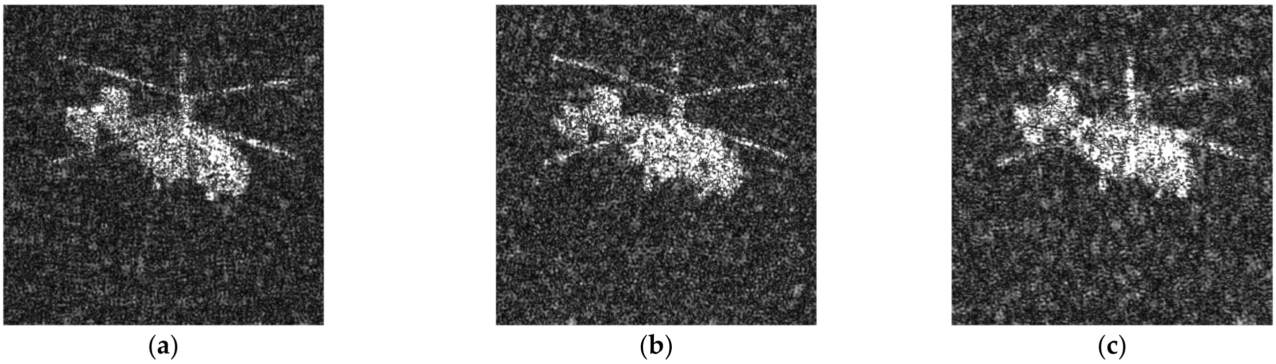

Figure 16. Radar images obtained for the square trajectory with variations: (**a**) 2.5 mm; (**b**) 5 mm; (**c**) 7.5 mm.

Since trajectory variations deteriorate the quality of the obtained image, the limiting factors of the variations were investigated by computing the MSE for variations from 0.1 mm to 10 mm, averaging 500 estimations for each variation value employed. Figure 17 shows the dependence of the MSE on the value of the variation of the radio scanner trajectory for moving in a square shape.

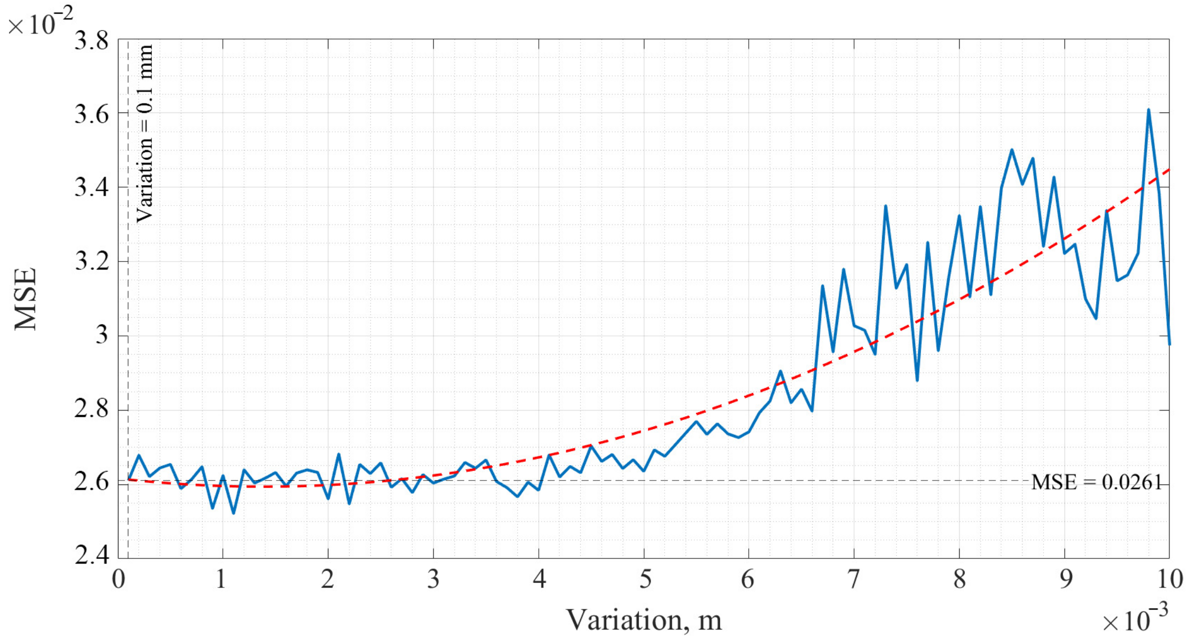

Figure 17. MSE errors as function of the radio scanner trajectory variations (red line represents the trend of MSE increase over the variation value).

Based on the obtained results, it can be concluded that to restore radio images of a static scene with dimensions of 0.5 m $\times$ 0.5 m (which are also the limits of the radio scanner's movement) at a height of 0.25 m and a signal frequency of 3 GHz, the accuracy of the radio scanner's movement should be at least 5 mm for the best output result. Currently, modern numerically controlled machines can position a sensor with millimetric precision. Therefore, it is technically possible to fulfill this movement variation constraint. Nevertheless, the list of radio scanner trajectories and their ambiguity functions presented and studied in this work is not exhaustive, and further simulation scenarios should be investigated. This manuscript is limited to studying a specific list of cases; however, future research will focus on analyzing a broader range of simulation cases.

4. Conclusions

This study develops a method for optimal coherent radar surface imaging using static-aperture synthesis technology. Unlike existing ones, this technology allows radio imaging of a stationary area with high resolution in range and azimuth due to coherent spatiotemporal processing of continuous signals in complex nonlinear radar sensor motion trajectories.

The classical principles of radar systems for coherent surface imaging from moving carriers have been developed, and principal procedures in processing for a radar system with the static-aperture technique that improve the quality of high-precision radio imaging for a fixed observation area have been designed. The novel framework for radio imaging has demonstrated good general operability and efficiency during simulation modeling for real sensing scenes. The cases of test image recovery for 10 different trajectories (Figures 4–13) of the system motion were modeled (according to the diagram in Figure 3), which implements the static-aperture synthesis method developed in this article. Based on the obtained simulation results (Figure 14), the reference metrics were calculated (Table 1). According to two of the three metrics (MSE and PSNR), the best trajectory among the presented ones is the square motion trajectory, whose improvement over the linear trajectory in MSE is 28.5%, and PSNR is 10%. The hourglass-shape motion trajectory also showed excellent results: an improvement over the linear trajectory in MSE is 25%, PSNR is 9%, and SSIM is 7%. The study of the hourglass-shape motion trajectory, as the best of the presented trajectory, with the presence of variations from 0.1 to 10 mm, showed (Figure 17) that to achieve MSE values comparable to the level of the idealized trajectory, the accuracy of the system positioning on which the device antenna is located should not be worse than 5 mm. Also, based on the simulation results, it can be seen that using the developed method of aperture synthesis improves every metric compared with the classical method with a side-looking view mode.

This design forms the theoretical base for developing advanced high-precision radiovision systems for a stationary observation area, including laboratory prototypes of aerospace remote-sensing radars and non-destructive testing radio systems applications. However, the proposed method, as well as all existing coherent radiovision methods based on aperture synthesis, can be affected by speckle noise, which may lead to incorrectly depicting the remotely sensed object. Another limitation of the proposed method is the positioning accuracy requirements of the radio sensor motion device. These requirements can specifically affect the study of large areas because, for example, rails of greater length have a more significant positioning variation along the axes. Therefore, in future investigations, we plan to employ the designed approach to other geometry-sensing configurations to improve radar imaging performance and perform experimental examinations of an imaging system prototype according to the developed block diagram in a real environment to calculate the marginal errors of the proposed method and mathematically and practically determine the limitations of its use.

Author Contributions: Methodology: O.I., D.K. (Danyil Kovalchuk), D.K. (Denys Kolesnikov), V.P. (Volodymyr Pavlikov), V.V. and S.Z.; formal analysis: O.I., D.K. (Denys Kolesnikov), D.K. (Danyil Kovalchuk), V.P. (Volodymyr Pavlikov), V.P. (Volodymyr Ponomaryov), V.V., B.G.-S. and S.Z.; investigation: D.K. (Denys Kolesnikov), D.K. (Danyil Kovalchuk), V.P. (Volodymyr Pavlikov), V.V. and S.Z.; resources: V.P. (Volodymyr Ponomaryov); data curation: D.K. (Denys Kolesnikov), D.K. (Danyil Kovalchuk), V.P. (Volodymyr Pavlikov), V.V. and S.Z.; writing—original draft preparation: O.I., D.K. (Denys Kolesnikov), V.P. (Volodymyr Pavlikov), V.P. (Volodymyr Ponomaryov), V.V., B.G.-S. and S.Z.; writing—review and editing: V.P. (Volodymyr Ponomaryov) and B.G.-S. All authors have read and agreed to the published version of the manuscript.

Funding: This research received no external funding.

Data Availability Statement: The original contributions presented in the study are included in the article; further inquiries can be directed to the corresponding author.

Acknowledgments: The authors would like to thank National Aerospace University "Kharkiv Aviation Institute" (Ukraine), Instituto Politecnico Nacional (IPN) (Mexico), Comision de Operacion y Fomento de Actividades Academicas (COFAA) of IPN, and Secretaria de Ciencia, Humanidades, Tecnologia e Innovacion (SECIHTI) (Mexico) for their support in this work.

Conflicts of Interest: The authors declare no conflicts of interest.

Abbreviations

The following abbreviations are used in this manuscript:

SAR	Synthetic-Aperture Radar
MLE	Maximum Likelihood Estimation
MIMO	Multiple-Input Multiple-Output
MSE	Mean Square Error
PSNR	Peak Signal-to-Noise Ratio
SSIM	Structural Similarity Index Measure
UAV	Unmanned Aerial Vehicle

Appendix A

Appendix A.1. Development of $R\left(\vec{r}, \vec{r}', \vec{r_t}\right)$ for the Fresnel Zone

The distance between any point within the scattered signal registration area and each point on the surface is represented as $R\left(\vec{r}, \vec{r}', \vec{r_t}\right)$ which is developed according to Equation (7) as follows:

$$R\left(\vec{r}, \vec{r}', \vec{r}_t\right) = R(x, y, x', y', x_t, y_t) = \sqrt{H^2 + [x - x_t + x']^2 + [y - y_t + y']^2}$$

$$= \sqrt{H^2 + [(x - x_t) + x']^2 + [(y - y_t) + y']^2}$$

$$= \sqrt{H^2 + (x - x_t)^2 - 2(x - x_t)x' + (x')^2 + (y - y_t)^2 - 2(y - y_t)y' + (y')^2}$$

$$= \sqrt{H^2 + (x - x_t)^2 + (y - y_t)^2 - 2(x - x_t)x' - 2(y - y_t)y' + (x')^2 + (y')^2}$$

$$= \sqrt{\left(R_0\left(\vec{r} - \vec{r}_t\right)\right)^2 - 2(x - x_t)x' - 2(y - y_t)y' + (x')^2 + (y')^2}$$

$$= R_0\left(\vec{r} - \vec{r}_t\right)\sqrt{1 + \frac{-2(x - x_t)x' - 2(y - y_t)y' + (x')^2 + (y')^2}{\left(R_0\left(\vec{r} - \vec{r}_t\right)\right)^2}}$$

Since $\sqrt{1 + x} = 1 + \frac{1}{2}x - \frac{1}{8}x^2 + \ldots$, if $|x| < 1$,

$$R\left(\vec{r}, \vec{r}', \vec{r}_t\right) \approx R_0\left(\vec{r} - \vec{r}_t\right)\left(1 + \frac{1}{2}\frac{-2(x - x_t)x' - 2(y - y_t)y' + (x')^2 + (y')^2}{\left(R_0\left(\vec{r} - \vec{r}_t\right)\right)^2}\right)$$

$$= R_0\left(\vec{r} - \vec{r}_t\right) - \frac{(x - x_t)x'}{R_0\left(\vec{r} - \vec{r}_t\right)} - \frac{(y - y_t)y'}{R_0\left(\vec{r} - \vec{r}_t\right)} + \frac{1}{2}\frac{(x')^2}{R_0\left(\vec{r} - \vec{r}_t\right)} + \frac{1}{2}\frac{(y')^2}{R_0\left(\vec{r} - \vec{r}_t\right)},$$

where

$$R_0\left(\vec{r} - \vec{r}_t\right) = R_0(x - x_t, y - y_t) = \sqrt{H^2 + (x - x_t)^2 + (y - y_t)^2} = \sqrt{H^2 + \left|\vec{r} - \vec{r}_t\right|^2}.$$

Appendix A.2. Development of Equation (40)

The development of the integral under the modulus sign in Equation (37), assuming scanning across all possible coordinates within the rectangular area D_t, is as follows:

$$\int_{D_{xt}}\int_{D_{yt}} e^{-j2\pi f_0 \frac{(x-x_{t_1})^2}{cH}} e^{-j2\pi f_0 \frac{(y-y_{t_1})^2}{cH}} e^{j2\pi f_0 \frac{(x_1-x_{t_1})^2}{cH}} \times$$

$$e^{j2\pi f_0 \frac{(y_1-y_{t_1})^2}{cH}} dx_{t_1}\, dy_{t_1} = \int_{-\frac{D_{xt}}{2}}^{\frac{D_{xt}}{2}} e^{-j2\pi f_0 \frac{(x-x_{t_1})^2}{cH}}$$

$$\times e^{j2\pi f_0 \frac{(x_1-x_{t_1})^2}{cH}} dx_{t_1} \int_{-\frac{D_{yt}}{2}}^{\frac{D_{yt}}{2}} e^{-j2\pi f_0 \frac{(y-y_{t_1})^2}{cH}} e^{j2\pi f_0 \frac{(y_1-y_{t_1})^2}{cH}} dy_{t_1}$$

$$= \int_{-\frac{D_{xt}}{2}}^{\frac{D_{xt}}{2}} e^{-j2\pi f_0 \frac{x^2-2xx_{t_1}-x_1^2+2x_1x_{t_1}}{cH}} dx_{t_1} \int_{-\frac{D_{yt}}{2}}^{\frac{D_{yt}}{2}} e^{-j2\pi f_0 \frac{y^2-2yy_{t_1}-y_1^2+2y_1y_{t_1}}{cH}} dy_{t_1}$$

$$= e^{-j2\pi f_0 \frac{x^2-x_1^2}{cH}} \int_{-\frac{D_{xt}}{2}}^{\frac{D_{xt}}{2}} e^{j2\pi f_0 \frac{2(x-x_1)x_{t_1}}{cH}} dx_{t_1} e^{-j2\pi f_0 \frac{y^2-y_1^2}{cH}}$$

$$\times \int_{-\frac{D_{yt}}{2}}^{\frac{D_{yt}}{2}} e^{j2\pi f_0 \frac{2(y-y_1)y_{t_1}}{cH}} dy_{t_1} = e^{-j2\pi f_0 \frac{x^2-x_1^2}{cH}} \left[\frac{e^{j2\pi f_0 \frac{2(x-x_1)}{cH} \frac{D_{xt}}{2}}}{j2\pi f_0 \frac{2(x-x_1)}{cH}} - \frac{e^{-j2\pi f_0 \frac{2(x-x_1)}{cH} \frac{D_{xt}}{2}}}{j2\pi f_0 \frac{2(x-x_1)}{cH}} \right]$$

$$\times e^{-j2\pi f_0 \frac{y^2-y_1^2}{cH}} \left[\frac{e^{j2\pi f_0 \frac{2(y-y_1)}{cH} \frac{D_{yt}}{2}}}{j2\pi f_0 \frac{2(y-y_1)}{cH}} - \frac{e^{-j2\pi f_0 \frac{2(y-y_1)}{cH} \frac{D_{yt}}{2}}}{j2\pi f_0 \frac{2(y-y_1)}{cH}} \right]$$

$$= e^{-j2\pi f_0 \frac{x^2-x_1^2}{cH}} \left[\frac{e^{j2\pi f_0 \frac{x-x_1}{cH} D_{xt}} - e^{-j2\pi f_0 \frac{x-x_1}{cH} D_{xt}}}{2j} \frac{1}{\pi f_0 \frac{2(x-x_1)}{cH}} \right]$$

$$\times e^{-j2\pi f_0 \frac{y^2-y_1^2}{cH}} \left[\frac{e^{j2\pi f_0 \frac{y-y_1}{cH} D_{yt}} - e^{-j2\pi f_0 \frac{y-y_1}{cH} D_{yt}}}{2j} \frac{1}{\pi f_0 \frac{2(y-y_1)}{cH}} \right]$$

$$= e^{-j2\pi f_0 \frac{x^2-x_1^2}{cH}} \left[\frac{\sin\left(2\pi f_0 \frac{x-x_1}{cH} D_{xt}\right)}{2\pi f_0 \frac{x-x_1}{cH}} \right] \frac{D_{xt}}{D_{xt}} e^{-j2\pi f_0 \frac{y^2-y_1^2}{cH}} \left[\frac{\sin\left(2\pi f_0 \frac{y-y_1}{cH} D_{yt}\right)}{2\pi f_0 \frac{y-y_1}{cH}} \right] \frac{D_{yt}}{D_{yt}}$$

$$= e^{-j2\pi f_0 \frac{x^2-x_1^2}{cH}} e^{-j2\pi f_0 \frac{y^2-y_1^2}{cH}} D_{xt} \sin c\left(2\pi f_0 \frac{x-x_1}{cH} D_{xt}\right) D_{yt} \sin c\left(2\pi f_0 \frac{y-y_1}{cH} D_{yt}\right).$$

References

1. Liu, W.; Ma, L.; Wang, J.; Chen, H. Detection of Multiclass Objects in Optical Remote Sensing Images. *IEEE Geosci. Remote Sens. Lett.* **2019**, *16*, 791–795. [CrossRef]
2. Seydi, S.T.; Hasanlou, M.; Amani, M.; Huang, W. Oil Spill Detection Based on Multiscale Multidimensional Residual CNN for Optical Remote Sensing Imagery. *IEEE J. Sel. Top. Appl. Earth Obs. Remote Sens.* **2021**, *14*, 10941–10952. [CrossRef]
3. Mied, R.P.; Chen, W.; Smith, G.B.; Wagner, E.J.; Miller, W.D.; Snow, C.M.; Marmorino, G.O.; Rhea, W.J. Airborne Remote Sensing of Surface Velocities in a Tidal River. *IEEE Trans. Geosci. Remote Sens.* **2018**, *56*, 4559–4567. [CrossRef]
4. Marmorino, G.O.; Smith, G.B.; Miller, W.D. Infrared Remote Sensing of Surf-Zone Eddies. *IEEE J. Sel. Top. Appl. Earth Obs. Remote Sens.* **2013**, *6*, 1710–1718. [CrossRef]
5. Sun, H.; Shimada, M.; Xu, F. Recent Advances in Synthetic Aperture Radar Remote Sensing—Systems, Data Processing, and Applications. *IEEE Geosci. Remote Sens. Lett.* **2017**, *14*, 2013–2016. [CrossRef]
6. Dell'Acqua, F.; Bignami, C.; Chini, M.; Lisini, G.; Polli, D.A.; Stramondo, S. Earthquake Damages Rapid Mapping by Satellite Remote Sensing Data: L'Aquila April 6th, 2009 Event. *IEEE J. Sel. Top. Appl. Earth Obs. Remote Sens.* **2011**, *4*, 935–943. [CrossRef]
7. Jiang, X.; Li, G.; Liu, Y.; Zhang, X.-P.; He, Y. Change Detection in Heterogeneous Optical and SAR Remote Sensing Images via Deep Homogeneous Feature Fusion. *IEEE J. Sel. Top. Appl. Earth Obs. Remote Sens.* **2020**, *13*, 1551–1566. [CrossRef]

8. Xia, Y.; Zhang, H.; Zhang, L.; Fan, Z. Cloud Removal of Optical Remote Sensing Imagery with Multitemporal SAR-Optical Data Using X-MTGAN. In Proceedings of the IGARSS 2019—2019 IEEE International Geoscience and Remote Sensing Symposium, Yokohama, Japan, 28 July–2 August 2019; pp. 3396–3399. [CrossRef]
9. Joshi, N.; Baumann, M.; Ehammer, A.; Fensholt, R.; Grogan, K.; Hostert, P.; Jepsen, M.R.; Kuemmerle, T.; Meyfroidt, P.; Mitchard, E.T.A.; et al. A Review of the Application of Optical and Radar Remote Sensing Data Fusion to Land Use Mapping and Monitoring. *Remote Sens.* **2016**, *8*, 70. [CrossRef]
10. Jung, H.-S.; Yun, S.-H.; Jo, M.-J. An Improvement of Multiple-Aperture SAR Interferometry Performance in the Presence of Complex and Large Line-of-Sight Deformation. *IEEE J. Sel. Top. Appl. Earth Obs. Remote Sens.* **2015**, *8*, 1743–1752. [CrossRef]
11. Guo, Q.; He, M.; Li, A. High-Resolution Remote-Sensing Image Registration Based on Angle Matching of Edge Point Features. *IEEE J. Sel. Top. Appl. Earth Obs. Remote Sens.* **2018**, *11*, 2881–2895. [CrossRef]
12. Chen, J.; Liang, B.; Zhang, J.; Yang, D.-G.; Deng, Y.; Xing, M. Efficiency and Robustness Improvement of Airborne SAR Motion Compensation with High Resolution and Wide Swath. *IEEE Geosci. Remote Sens. Lett.* **2022**, *19*, 4004005. [CrossRef]
13. Santosa, B.H.; Marpaung, F. Wetlands Delineation with Various Land Covers Using SAR Sentinel-1A Surface Backscatter Ratio. *J. Teknol. Lingkung.* **2022**, *23*, 1–11. [CrossRef]
14. Wang, Z.; Gogineni, S.; Rodriguez-Morales, F.; Yan, J.-B.; Paden, J.; Leuschen, C.; Hale, R.D.; Li, J.; Carabajal, C.L.; Gomez-Garcia, D.; et al. Multichannel Wideband Synthetic Aperture Radar for Ice Sheet Remote Sensing: Development and the First Deployment in Antarctica. *IEEE J. Sel. Top. Appl. Earth Obs. Remote Sens.* **2016**, *9*, 980–993. [CrossRef]
15. Lopez-Sanchez, J.M.; Ballester-Berman, J.D. Potentials of Polarimetric SAR Interferometry for Agriculture Monitoring. *Radio Sci.* **2009**, *44*, 1–20. [CrossRef]
16. Takahashi, K.; Matsumoto, M.; Sato, M. Continuous Observation of Natural-Disaster-Affected Areas Using Ground-Based SAR Interferometry. *IEEE J. Sel. Top. Appl. Earth Obs. Remote Sens.* **2013**, *6*, 1286–1294. [CrossRef]
17. Dou, H.; Li, H.; He, Z.; Wu, Y.; Lv, R.; Li, Y.; Song, G.; Li, Q.; Chen, K.; Gui, L.; et al. Analysis and Correction of the Phase and Amplitude Errors for Mirrored Aperture Synthesis. *IEEE Geosci. Remote Sens. Lett.* **2022**, *19*, 8012905. [CrossRef]
18. Feng, L.; Wu, M.; Li, Q.; Chen, K.; Li, Y.; He, Z.; Tong, J.; Tu, L.; Xie, H.; Lu, H. Array Factor Forming for Image Reconstruction of One-Dimensional Nonuniform Aperture Synthesis Radiometers. *IEEE Geosci. Remote Sens. Lett.* **2016**, *13*, 237–241. [CrossRef]
19. Kraus, J.D. *Radio Astronomy*; McGraw-Hill: New York, NY, USA, 1966.
20. Lovell, B.; Clegg, J.A. *Radio Astronomy*; Oxford University Press: Oxford, UK, 1975.
21. Chen, X.; Kildal, P.-S.; Carlsson, J.; Yang, J. Comparison of Ergodic Capacities From Wideband MIMO Antenna Measurements in Reverberation Chamber and Anechoic Chamber. *IEEE Antennas Wirel. Propag. Lett.* **2011**, *10*, 446–449. [CrossRef]
22. Wang, X.; Vick, R. Determination of Radiated Emissions of an Electrically Large EUT: Simulation and Experiment. *IEEE Electromagn. Compat. Mag.* **2017**, *6*, 32–35. [CrossRef]
23. Kim, B.K.; Kang, H.-S.; Park, S.-O. Experimental Analysis of Small Drone Polarimetry Based on Micro-Doppler Signature. *IEEE Geosci. Remote Sens. Lett.* **2017**, *14*, 1670–1674. [CrossRef]
24. Song, Y.; Wang, S.; Li, Q.; Mu, H.; Feng, R.; Tian, T.; Tian, J. Vehicle Target Detection Method for Wide-Area SAR Images Based on Coarse-Grained Judgment and Fine-Grained Detection. *Remote Sens.* **2023**, *15*, 3242. [CrossRef]
25. Lin, X.; Zhang, B.; Wu, F.; Wang, C.; Yang, Y.; Chen, H. SIVED: A SAR Image Dataset for Vehicle Detection Based on Rotatable Bounding Box. *Remote Sens.* **2023**, *15*, 2825. [CrossRef]
26. Amjadipour, F.; Imani, M.; Ghassemian, H. Morphological and Statistical Filter-Based Multi-Direction Building Detection for SAR Images. *J. Appl. Res. Electr. Eng.* **2023**, *2*, 145–151. [CrossRef]
27. Cooper, K.B.; Dengler, R.J.; Llombart, N.; Thomas, B.; Chattopadhyay, G.; Siegel, P.H. THz Imaging Radar for Standoff Personnel Screening. *IEEE Trans. Terahertz Sci. Technol.* **2011**, *1*, 169–182. [CrossRef]
28. Daniels, D.J. Radar for Non-Destructive Testing of Materials. In Proceedings of the IEE Colloquium on Measurements, Modelling and Imaging for Non-Destructive Testing, London, UK, 27 March 1991; pp. 9/1–9/3.
29. García-Rial, F.; Úbeda-Medina, L.; Grajal, J.; Badolato, A.; Rubio-Cidre, G.; Garcia-Pino, A.; Gonzalez-Valdes, B.; Rubiños, O. Optimization of a Compact THz Imaging Radar for Real-Time Operation. In Proceedings of the 2016 Global Symposium on Millimeter Waves (GSMM) & ESA Workshop on Millimeter-Wave Technology and Applications, Espoo, Finland, 6–8 June 2016; pp. 1–4. [CrossRef]
30. Charvat, G.L. *Small and Short-Range Radar Systems*; Modern and Practical Approaches to Electrical Engineering; CRC Press: Boca Raton, FL, USA, 2014.
31. Falkovich, S.E.; Ponomaryov, V.I.; Shkvarko, Y.V. *Optimal Reception of Space-Time Signals in Channels with Scattering*; Radio and Communication: Moscow, Russia, 1989.
32. Charvat, G.L.; Kempel, L.C.; Rothwell, E.J.; Coleman, C.M.; Mokole, E.L. A Through-Dielectric Radar Imaging System. *IEEE Trans. Antennas Propag.* **2010**, *58*, 2594–2603. [CrossRef]
33. Charvat, G.L.; Kempel, L.C.; Rothwell, E.J.; Coleman, C.M.; Mokole, E.L. A Through-Dielectric Ultrawideband (UWB) Switched-Antenna-Array Radar Imaging System. *IEEE Trans. Antennas Propag.* **2012**, *60*, 5495–5500. [CrossRef]

34. Volosyuk, V.K.; Zhila, S.S.; Kolesnikov, D.V. Phenomenological Description of Coherent Radar Images Based on the Concepts of the Measure of Set and Stochastic Integral. *Telecommun. Radio Eng.* **2019**, *78*, 19–30. [CrossRef]
35. Volosyuk, V.; Kravchenko, V. *Statistical Theory of Radio-Technical Systems of Remote Sensing and Radiolocation*; FIZMATLIT: Moscow, Russia, 2008.
36. Volosyuk, V.; Zhyla, S.; Pavlikov, V.; Vlasenko, D.; Kosharskiy, V.; Kolesnikov, D.; Inkarbaeva, O.; Nezhalskaya, K. Optimal Radar Cross Section Estimation in Synthetic Aperture Radar with Planar Antenna Array. *Radioelectron. Comput. Syst.* **2021**, *1*, 50–59. [CrossRef]
37. Sun, Y.; Jiang, W.; Yang, J.; Li, W. SAR Target Recognition Using cGAN-Based SAR-to-Optical Image Translation. *Remote Sens.* **2022**, *14*, 1793. [CrossRef]